UNIFORM WEIGHTED COMPACT / NON-COMPACT SCHEMES FOR SHOCK / BOUNDARY LAYER INTERACTION

by

PENG XIE

Presented to the Faculty of the Graduate School of

The University of Texas at Arlington in Partial Fulfillment

of the Requirements

for the Degree of

DOCTOR OF PHILOSOPHY

THE UNIVERSITY OF TEXAS AT ARLINGTON

DECEMBER 2007

ACKNOWLEDGEMENTS

This dissertation could not have been written without Dr. Chaoqun Liu who not only served as my supervisor but also encouraged me throughout my academic program.

I also want to thank Dr. Jiangang Cai who, over the last three years, was always ready to provide me with the most generous help in every single aspect. I am also indebted to Dr. Li Jiang and Dr. Hua Shan who kindly answered all kinds of questions from me. My work was based on their previous FORTRAN codes which are absolutely the best codes I have ever seen. I want to thank Dr. Jianzhong Su, Dr. Hristo Kojouharov and Dr. Guojun Liao for serving as my committee members and reviewing my dissertation.

I also want to say thank you to my loving and beloved wife who supports me constantly, selflessly and unconditionally.

December 14, 2007

ABSTRACT

UNIFORM WEIGHTED COMPACT / NON-COMPACT

SCHEMES FOR SHOCK / BOUNDARY

LAYER INTERACTION

Publication No. _____

Peng Xie, PhD.

The University of Texas at Arlington, 2007

Supervising Professor: Chaoqun Liu

The critical problem of CFD is perhaps an accurate approximation of derivatives for a given discrete data set. Based on our previous work on the weighted compact scheme (WCS), a uniform weighted compact / non-compact scheme (UWCNC) has been developed. Similar to WENO, three high order candidates, left, right, and central, are constructed by using Hermite polynomials. According to the smoothness, three weights are derived and assigned to each candidate. The weights will lead the scheme to be upwind-biased when approaching the shock or other

discontinuities but quickly becomes central, compact, and of high order just off the shock. Therefore, the new scheme can get a sharp shock without oscillation, but keep central, compact and of high resolution in the smooth area. This feature is particularly important to numerical simulation of the shock-boundary layer interaction, where both shock and small eddies are important. Comparing with 5th order WENO which has 5th order accuracy in the smooth area and 3rd order accuracy near the shock, UWCNC scheme is superior with smaller stencils and higher order of accuracy. The necessary dissipation is provided by weights and some high order upwind-biased scheme. The new scheme has been successfully applied to 1-Dimensional shock tube and shock-entropy interaction and 2-Dimensional incident shock reflection. The new scheme has obtained sharper shock, no deformation of expansion wave, and much higher resolution than 5th order WENO for small length scales. A variety of cases including shock-boundary interaction with incident shock and double angles has been tested. The preliminary numerical solution is encouraging.

TABLE OF CONTENTS

LIST OF ILLUSTRATIONS

LIST OF TABLES

CHAPTER 1

INTRODUCTION

1.1 Overview on shock capturing schemes

The fluid flow is in general governed by the Navier-Stokes equation which is a system of time dependent partial differential equations. However, for external flow, the viscosity is important largely only in the boundary layers. The main flow can still be considered as inviscid and the governing system can be dominated by the time dependent Euler equations which are hyperbolic. The difficult problem with numerical solution is to capture shocks which can be considered as a discontinuity or mathematical singularity (no classical unique solution and no bounded derivatives). In the shock area, continuity and differentiability of the governing Euler equations are lost and only the weak solution in an integration form can be obtained. The shock can be developed in some cases because the Euler equation is non-linear and hyperbolic. On the other hand, the governing Navier-Stokes system presents parabolic type behaviors and is therefore dominated by viscosity or second order derivatives. One expects that the equation should be solved by high order central difference scheme, high order compact scheme is preferable, to get high order of accuracy and high resolution. High order of accuracy is critical in resolving small length scales in flow transition and

turbulence process. However, for the hyperbolic system, the analysis already shows the existence of characteristic lines and Riemann invariants. Apparently, the upwind finite difference scheme coincides with the physics for a hyperbolic system. History has shown the great success of upwind technologies. We should consider not only the eigenvalues and eigenvectors of the Jacobian system, but also non-linearity including the Rankine-Hugoniot shock relations. From the point of view of shocks, it makes no sense to use high order compact scheme for shock capturing which use all gird points on one grid line to calculate the derivative by solving a tri-diagonal or penta-diagonal linear system because shock does not have finite derivatives and downstream quantities cannot cross shock to affect the upstream points. From the point of view of the above statement, upwind scheme is appropriate for the hyperbolic system. Many upwind or bias upwind schemes have achieved great success in capturing shocks sharply, such as Godunov (1959), Roe (1981), MUSCL (Van Leer, 1979), TVD (Harten, 1983), ENO (Harten et al, 1987; Shu et al, 1988, 1989) and WENO (Liu et al, 1994; Jiang et al, 1996). Roe's scheme may be better in capturing the shock sharply because it satisfies the Rankine-Hugoniot relation. Of course, Roe's method can also be considered as a method for flux difference splitting and any high order method such as ENO and WENO can use Roe's method as a splitting method. However, all these shock-capturing schemes are based on upwind or bias upwind technology, which is appropriate for hyperbolic system, but is not favorable to the N-S system which presents parabolic equation behavior. The small length scale is very important in the flow transition and turbulence process is thus very sensitive to any artificial numerical

dissipation. High order compact scheme (Lele, 1992; Visbal, 2002) is more appropriate for simulation of flow transition and turbulence because it is central and non-dissipative with high order accuracy and high resolution.

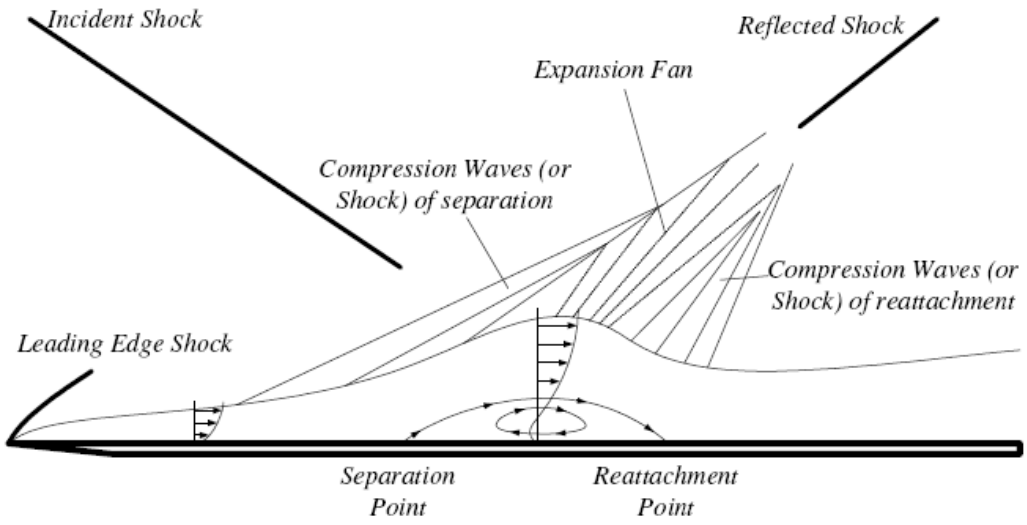

Figure 1.1 Schematic of the flow pattern of shock / boundary layer interaction

Unfortunately, the shock-boundary layer interaction, which is common and important in high speed flows, is a mixed type problem which has shock (discontinuity), boundary layer (viscosity), separation, transition, expansion fans, fully developed turbulence and reattachment. In order to capture the shock and keep high order accuracy and high resolution in the smooth area, we have developed the so called weighted compact scheme (WCS, Jiang et al, 2001) which works very well for 1-D convection equation, Burger's equation, but not so good for Euler's equation with shocks. Visible wiggles have been found near the shock. In the case of shock-boundary layer

interaction, there are elliptic areas (separation, transition, turbulence) and hyperbolic areas (main flow, shocks, expansion fans), which make the accurate numerical simulation extremely difficult if not impossible. We have to divide the computational domain to several parts: the elliptic, hyperbolic, and mixed regions. The division or detection can be performed by switch function automatically such as shock detector which simply sets $\Omega = 1$ for the shock area and $\Omega = 0$ for the rest. The switch function may give the best results for shock-boundary layer interaction, but it will have too many logical statements in the code which may slow down the computation. The switch function could also be case-related and very difficult to adjust. It would also slow down the convergence for steady problems. The use of "weights" will be naturally considered as a good candidate that succeeded for many schemes, WENO is a good example and Weighted Compact Scheme is another example.

Traditional finite difference schemes use the idea of Lagrange interpolation. To obtain nth order of accuracy, a stencil covering n+1 grid points is needed. In other words, the derivative at a certain grid point depends upon the function values at these n+1 grid points and only these grid points. In contrast, standard compact schemes (Lele, 1992; Visbal, 2002) use the idea of Hermitian interpolation. By using derivatives as well as function values, a compact scheme achieves high order of accuracy without increasing the width of stencils. As discussed in Lele's paper, a compact scheme has not only high order of accuracy, but also high resolution. Fourier analysis indicates that, with the same order of accuracy, a compact scheme has better spectral resolution than a

traditional, explicit finite difference scheme. For this reason, compact schemes are favorable in the simulation of turbulent flows where small-length-scale structures are important.

Due to the usage of derivatives, compact schemes usually give us a tri-diagonal or penta-diagonal system. Although the tri-diagonal matrix is sparse, the inverse of a tri-diagonal matrix is dense, which means the derivative at a certain grid point depends upon all the grid points along a grid line. The success of compact schemes indicates that the global dependency is very important for high resolution. However, the global dependency is good for resolution but not so applicable for shock capturing.

The basic idea proposed in ENO (Harten et al, 1987) and WENO (Jiang et al, 1996) schemes is to avoid the stencil containing a shock. ENO chooses the smoothest stencil from several candidates to calculate the derivatives. WENO controls the contributions of different stencils according to their smoothness. In this way, the derivative at a certain grid point, especially one near the shock, is dependent on a very limited number of grid points. The local dependency here is favorable for shock capturing and helps obtaining the non-oscillatory property. The success of ENO and WENO schemes indicates that the local dependency is critical for shock capturing.

The Weighted Compact Scheme (WCS) developed by Jiang et al, 2001 is constructed by introducing the idea of WENO scheme to the standard compact schemes

which uses weights for several candidates. The building block for each candidate is a Lagrange polynomial in WENO, but is Hermite in WCS. Therefore WCS achieves a higher accuracy with same stencil width. In shock regions, WCS controls the contributions of different candidate stencils to minimize the influence of the candidate which contains a shock. In smooth regions where shocks are not present, WCS recovers to the standard compact scheme to achieve high accuracy and resolution. The numerical tests indicate that original WCS works fine in some cases such as convection equation and Burger's equation, but not very well for Euler equation. As mentioned above, the usage of derivatives by compact schemes results in the global dependency.

In order to overcome the drawback of the WCS scheme, we need to achieve local dependency in shock regions and recover the global dependency in smooth regions. This fundamental idea will naturally lead to a combination of local dependent scheme, e.g. WENO and global dependent weighted compact schemes which we call "Uniform Weighted Compact / Non-compact Schemes" (UWCNC). The mixing and weights are designed in following ways: the new scheme automatically becomes bias when approaching the shock, but rapidly recovers to be central, compact, with high order of accuracy and high resolution. This kind of scheme has been developed and preliminary computation results are very promising.

1.2 Importance of high order schemes to DNS/LES

It should be pointed out that the order of accuracy of the finite difference scheme is absolutely not a trivial issue to CFD, especially to DNS and LES. There is a

significant difference in requirements of grid size by DNS/LES between low order schemes and high order schemes. Let us take a look at the local truncation error for 1-D problem. If one uses a second order scheme with a mesh size of Δx_2 and wants to have same truncation error using a sixth order scheme with a mesh size of Δx_6, one should have:

$$C_2(\Delta x_2)^2 = C_6(\Delta x_6)^6 \tag{1.1}$$

Assume $C_2 \approx C_6$ and $\Delta x_6 = 0.01$ (100 grid points in a normalized domain), we will get

$$(\Delta x_2)^2 = (10^{-2})^6$$

$$\Delta x_2 = 10^{-6} \tag{1.2}$$

In other words, the second order scheme needs one million of grid points to beat the sixth order scheme with 100 grid points for same order of accuracy. This advantage of high order scheme will become more significant when one uses DNS for 3-D problems. We do not want to use one million of grids in each direction for DNS, but prefer to use 100 grid points. Therefore high order scheme must be used. Of course, the global accuracy is also influenced by factors other than the local truncation errors, and the advantage of the sixth order scheme does not typically show a magnitude of 10 thousand times improvement over the second order scheme. However, it is now widely recognized that high order finite schemes are strongly encouraged to be used for DNS and LES which have much higher accuracy and higher resolution than low order schemes.

1.3 Discussion on low order LES with low order subgrid models

Most LES computations require use of a subgrid model trying to get the unresolved scales back, which could be mathematically considered as truncation errors. Let us take a look at the famous Smagorinsky model:

$$t_{ij} = -n_t S_{ij} \text{ and}$$
$$n_t = C_s \Delta)^2 \mid S \mid \qquad (1.3)$$

Where $t_{ij}, S_{ij}, C_s, \Delta$ are unresolved stress tensor, resolved strain tensor, Smagorinsky constant, and filter width, respectively. Apparently, it is a second order model with Δ^2. Other models are similar. If we use a sixth order compact scheme for LES without model (Implicit LES), we will get sixth order of accuracy. However, if we add the Smgorinsky subgrid model, our LES results will be degenerated to second order of accuracy, which is really bad. A carefully designed 6th order subgrid model may be needed for high order LES. Therefore, second order DNS, second order LES with second order subgrid models are not appropriate for DNS or LES.

Table 1 shows the orders obtained by different orders of schemes, which demonstrates the importance of high order numerical schemes for DNS/LES.

Table 1.1 Orders of DNS/LES approaches

Scheme	Truncation Errors	Comments
Second order DNS	$O(h^2)$	Bad
Second order LES +Second order subgrid model	$O(h^2)$ or up	Bad
Sixth order LES without subgrid model (ILES)	$O(h^6)$	Good

Table 1.1 - Continued

Sixth order LES with second order subgrid model	$O(h^2)$	Bad
Sixth order LES with sixth order subgrid model	$O(h^6)$ or up	Best

1.4 Basic point of view on the scheme development

The 3-D time dependent Navier-Stokes equations in a general curvilinear coordinate can be written as

$$\frac{1}{J}\frac{\partial Q}{\partial t}+\frac{\partial(E-E_v)}{\partial x}+\frac{\partial(F-F_v)}{\partial h}+\frac{\partial(F-F_v)}{\partial z}=0 \tag{1.4}$$

For 1-D conservation law, it will be:

$$\frac{\partial Q}{\partial t}+\frac{\partial E}{\partial x}=0 \tag{1.5}$$

The critical issue for high order CFD is to find an accurate approximation of derivatives for a given discrete data set. The computer does not know any physical process but accepts a discrete data set as input. The output is also a discrete data set. We measure the input data by slopes to determine it is smooth (slope is small), oscillatory (slope is large), and non-differentiable (or corner points which have slopes large on one side, but small on the other side), or, in other words, by a smoothness function, and then an appropriate numerical scheme is set up based on the feature of the discrete data set, but not the governing system. This is the basic view point for our new scheme development.

CHAPTER 2

UNIFORM WEIGHTED COMPACT / NON-COMPACT SCHEMES

2.1 ENO reconstruction function

For 1-D conservation laws:

$$u_t(x,t) + f_x(u(x,t)) = 0 \tag{2.1}$$

When a conservative approximation to the spatial derivative is applied, a semi-discrete conservative form of the equation (2.1) is described as follows:

$$\frac{du_j}{dt} = -\frac{1}{\Delta x}(\hat{f}_{j+(1/2)} - \hat{f}_{j-(1/2)}) \tag{2.2}$$

where $f_j = \frac{1}{\Delta x}\int_{x_j-\Delta x/2}^{x_j+\Delta x/2} \hat{f}(x)dx$ and then $(f_x)_j = -\frac{1}{\Delta x}(\hat{f}_{j+(1/2)} - \hat{f}_{j-(1/2)})$. Note that f is the original function, but $\hat{f}$ is the flux defined by the above integration which is an exact expression of the flux but is different from *f*.

Let H be the primitive function of $\hat{f}$ defined below:

$$H(x_{j+(1/2)}) = \int_{-\infty}^{x_j+\Delta x/2} \hat{f}(x)dx = \sum_{i=-\infty}^{i=j} \int_{x_i-\Delta x/2}^{x_i+\Delta x/2} \hat{f}(x)dx = \Delta x \sum_{i=-\infty}^{j} f_i \tag{2.3}$$

H can be easily calculated, but is a discrete data set.

The numerical flux $\hat{f}$ at the cell interfaces is the derivative of its primitive function *H*. i.e.:

$$\hat{f}_{j+(1/2)} = H'_{j+(1/2)} \tag{2.4}$$

All formulae given above are exact without approximations. However, the primitive function H is a discrete data set or discrete function and we have to use numerical method to get the derivatives, which will introduce numerical errors, or, in other words, order of accuracy.

This procedure, $f \to H \to \hat{f} \to f'_x$, is called reconstruction introduced by Shu & Osher (1988, 1989). The problem left for numerical methods is how to solve (2.4) or how to get accurate derivatives for a data set.

2.2 Data normalization

In order to find universal formula, we need to normalize the data set, u(i), i=1, …, n:

$$u_{diff} = | u_{\max} - u_{\min} | \tag{2.5}$$

$$\bar{u} = (u - u_{\min}) / u_{diff} \tag{2.6}$$

Here, $u_{\max}$ and $u_{\min}$ are the maximum and minimum values of u respectively and $\bar{u}$ is normalized. For simplicity, we throw out the hat of u and use u(i) as the normalized data set.

2.3 Weighted compact scheme

As we addressed that one problem left for numerical methods, which is how to solve (2.4) or how to get accurate derivatives for a discrete data set. It is equivalent to

finding an accurate flux in the interface. We turn our attention into finding a high order scheme which, however, must be able to pass the shock without non-physical wiggles.

2.3.1 WENO Scheme (Jiang & Su, 1996)

Before discuss our new scheme, first let us see how to construct the WENO scheme.

2.3.1.1 Conservation Form of Derivative

$$\frac{\partial U}{\partial t}+\frac{\partial F}{\partial x}=0 \tag{2.7}$$

The ENO reconstruction can provide a semi-discretization for the derivative: $\frac{\partial F}{\partial x}=\frac{\hat{F}_{i+\frac{1}{2}}-\hat{F}_{i-\frac{1}{2}}}{\Delta x}$, where $\hat{F}$ is the flux which must be accurately obtained.

2.3.1.2 Fifth Order WENO (bias upwind)

1) Flux approximation

In order to get an high order approximation for $\hat{F}_{j-\frac{1}{2}}=H'_{j-\frac{1}{2}}$, we can use three different candidates (Figure 2.1) which are all third order polynomials: $E_0: H_{j-\frac{7}{2}}, H_{j-\frac{5}{2}}, H_{j-\frac{3}{2}}, H_{j-\frac{1}{2}}$; $E_1: H_{j-\frac{5}{2}}, H_{j-\frac{3}{2}}, H_{j-\frac{1}{2}}, H_{j+\frac{1}{2}}$; $E_2: H_{j-\frac{3}{2}}, H_{j-\frac{1}{2}}, H_{j+\frac{1}{2}}, H_{j+\frac{3}{2}}$.

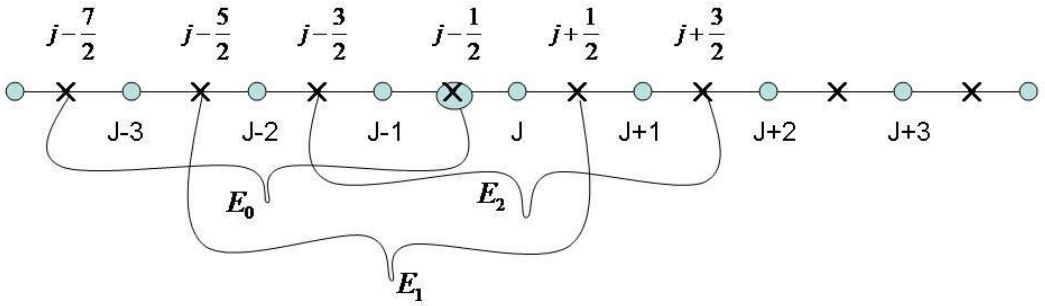

Figure 2.1 Schematics of WENO Scheme Stencils – WENO Candidates

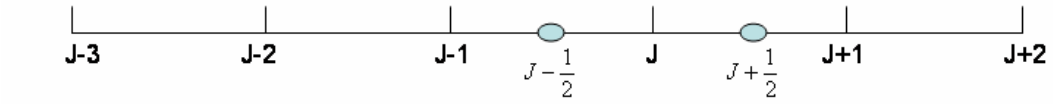

Figure 2.2 Schematics of WENO Scheme Stencils – 5th order WENO Scheme

Let us look at candidate E_0 first. Assume H is a third order polynomial: $H = a_0 + a_1(x - x_{j-1/2}) + a_2(x - x_{j-1/2})^2 + a_3(x - x_{j-3/2})^3$, we have

$$\begin{aligned} H_{j-1/2} &= a_0 \\ H_{j-3/2} &= a_0 - a_1 h + a_2 h^2 - a_3 h^3 \\ H_{j-5/2} &= a_0 - 2a_1 h + 4a_2 h^2 - 8a_3 h^3 \\ H_{j-7/2} &= a_0 - 3a_1 h + 9a_2 h^2 - 27a_3 h^3 \end{aligned} \tag{2.8}$$

Further by subtraction, we can get

$$\begin{aligned} H_{j-1/2} - H_{j-3/2} &= hF_{j-1} = a_1 h - a_2 h^2 + a_3 h^3 \\ H_{j-1/2} - H_{j-5/2} &= h(F_{j-1} + F_{j-2}) = 2a_1 h - 4a_2 h^2 + 8a_3 h^3 \\ H_{j-1/2} - H_{j-7/2} &= h(F_{j-1} + F_{j-2} + F_{j-3}) = 3a_1 h - 9a_2 h^2 + 27a_3 h^3 \end{aligned} \tag{2.9}$$

Deleting a_3, we can get

$$\begin{aligned} 8F_{j-1} - (F_{j-1} + F_{j-2}) &= 6a_1 - 4a_2 h \\ 27F_{j-1} - (F_{j-1} + F_{j-2} + F_{j-3}) &= 24a_1 - 18a_2 h \end{aligned} \tag{2.10}$$

or

$$\begin{aligned} 63F_{j-1} - 9F_{j-2} &= 54a_1 \\ 52F_{j-1} - 2F_{j-2} - 2F_{j-3} &= 48a_1 \end{aligned} \tag{2.11}$$

Then,

$$6a_1 = 2F_{j-3} - 7F_{j-2} + 11F_{j-1}$$

$$\text{Or} \quad E_0 : \hat{F}_{j-\frac{1}{2}} = H'_{j-1/2} = a_1 = \frac{1}{3}F_{j-3} - \frac{7}{6}F_{j-2} + \frac{11}{6}F_{j-1} \tag{2.12}$$

Finally, we have

$$\begin{aligned} E_0 : \hat{F}_{j-\frac{1}{2}} &= \frac{1}{3}F_{j-3} - \frac{7}{6}F_{j-2} + \frac{11}{6}F_{j-1} \\ E_1 : \hat{F}_{j-\frac{1}{2}} &= -\frac{1}{6}F_{j-2} + \frac{5}{6}F_{j-1} + \frac{1}{3}F_j \\ E_2 : \hat{F}_{j-\frac{1}{2}} &= \frac{1}{3}F_{j-1} + \frac{5}{6}F_j - \frac{1}{6}F_{j+1} \end{aligned} \tag{2.13}$$

2) Optimal weights for high order of accuracy

The final scheme should be a combination of three candidates: $E = C_0 E_0 + C_1 E_1 + C_2 E_2$. If we set $C_0 = \frac{1}{10}$, $C_1 = \frac{6}{10}$, $C_2 = \frac{3}{10}$, we will have

$$\hat{F}_{j-\frac{1}{2}} = \frac{1}{30}F_{j-3} - \frac{13}{60}F_{j-2} + \frac{47}{60}F_{j-1} + \frac{27}{60}F_j - \frac{1}{20}F_{j+1}$$

$$\hat{F}_{j+\frac{1}{2}} = \frac{1}{30}F_{j-2} - \frac{13}{60}F_{j-1} + \frac{47}{60}F_j + \frac{27}{60}F_{j+1} - \frac{1}{20}F_{j+2} \tag{2.14}$$

$$\frac{\partial F}{\partial x} = \frac{\hat{F}_{j+\frac{1}{2}} - \hat{F}_{j-\frac{1}{2}}}{\Delta x} = (-\frac{1}{30}F_{j-3} + \frac{1}{4}F_{j-2} - F_{j-1} + \frac{1}{3}F_j + \frac{1}{2}F_{j+1} - \frac{1}{20}F_{j+2})/\Delta x + O(\Delta x^5)$$

Using Taylor expansion for F_{j-k}, we find

$$\frac{\partial F}{\partial x} = \frac{\hat{F}_{j+\frac{1}{2}} - \hat{F}_{j-\frac{1}{2}}}{\Delta x} = F'_j - \frac{1}{60}(\Delta x)^5 F_j^{(6)} + \frac{1}{140}(\Delta x)^6 F_j^{(7)} + \ldots, \tag{2.15}$$

which shows the scheme with optimal weights and 6 grid points has a 5th order truncation error. Note that the scheme is a standard 5th order bias upwind finite difference scheme.

3) Bias up-wind weights:

Let us define a bias weight for each candidate according to WENO:

$$w_k = \frac{g_k}{\sum_{i=0}^{2} g_i}, \qquad g_k = \frac{C_k}{(e + IS_k)^p} \tag{2.16}$$

where

$$IS_i = \int_{x_{j-1/2}}^{x_{j+1/2}} \sum_{k=1}^{\infty} [p_2(x)^{(k)}]^2 h^{2k-1} dx$$

$$IS_0 = \frac{13}{12}(F_{j-2} - 2F_{j-1} + F_j)^2 + \frac{1}{4}(F_{j-2} - 4F_{j-1} + 3F_j)^2$$

$$IS_1 = \frac{13}{12}(F_{j-1} - 2F_j + F_{j+1})^2 + \frac{1}{4}(F_{j-1} - F_{j+1})^2$$

$$IS_2 = \frac{13}{12}(F_j - 2F_{j+1} + F_{j+2})^2 + \frac{1}{4}(F_{j+2} - 4F_{j+1} + 3F_j)^2$$

The 5th order WENO can be obtained

$$\hat{F}_{j-1/2} = w_0 E_0 + w_1 E_1 + w_2 E_2 \tag{2.17}$$

$$\begin{aligned}\hat{F}_{j-1/2} = {} & w_{0,j-1/2}\left(\frac{1}{3}F_{j-3} - \frac{7}{6}F_{j-2} + \frac{11}{6}F_{j-1}\right) + w_{1,j-1/2}\left(-\frac{1}{6}F_{j-2} + \frac{5}{6}F_{j-1} + \frac{1}{3}F_j\right) \\ & + w_{2,j-1/2}\left(\frac{1}{3}F_{j-1} + \frac{5}{6}F_j - \frac{1}{6}F_{j+1}\right)\end{aligned} \tag{2.18}$$

WENO is a very popular scheme with great successes by many users. However, the scheme has 5th order dissipation everywhere and third order dissipation near the shock and it is too dissipative for transition and turbulence. Let us turn into central and compact schemes for assistance.

2.3.2 Weighted Compact Scheme (WCS, Jiang et al, 2001)

1) High-order compact schemes

A Pade-type compact scheme could be constructed based on the Hermite interpolation where both function and derivatives at grid points are involved, e.g. a fourth order finite difference scheme can be constructed if both the function and first order derivative are used at three grid points. For a function f we may write a compact scheme by using five grid points (Lele, 1992):

$$b_- f'_{j-2} + a_- f'_{j-1} + f'_j + a_+ f'_{j+1} + b_+ f'_{j+2} = (b_- f_{j-2} + a_- f_{j-1} + c f_j + a_+ f_{j+1} + b_+ f_{j+2})/\Delta x \tag{2.19}$$

We can get 8th order of accuracy by using the above formula based on Taylor series.

If we use a symmetric and tri-diagonal system, by setting $b_- = b_+ = 0$, we can get a one parameter family of compact scheme (Lele, 1992):

$$a\ f'_{i-1} + f'_i + a\ f'_{i+1} = \left[-\frac{1}{12}(4a-1) f_{i-2} - \frac{1}{3}(a+2) f_{j-1} + \frac{1}{3}(a+2) f_{j+1} + \frac{1}{12}(4a-1) f_{i+2} \right] / h \quad (2.20)$$

If $a = \frac{1}{3}$, we will get a standard sixth order compact scheme.

When a compact scheme is used to differentiate a discontinuous or shock function, the computed derivative has grid to grid oscillations. In our previous work (Jiang et al, 2001) a new class of finite difference scheme - weighted compact scheme (WCS) was proposed.

2) Basic formulations of weighted compact scheme

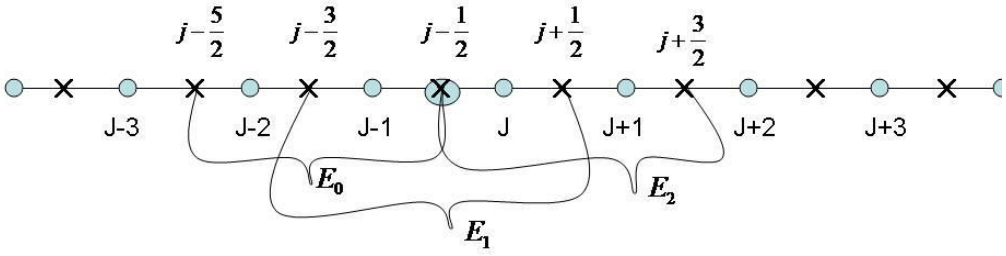

Figure 2.3 WCS Stencil Candidates

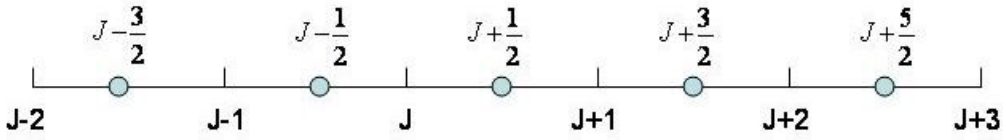

Figure 2.4 Sixth Order Compact Scheme

In order to get an high order approximation for $\hat{F}_{j-\frac{1}{2}} = H'_{j-\frac{1}{2}}$, the six order weighted compact scheme uses three candidates for $\hat{F}_{j-\frac{1}{2}}$ as shown in Figure 2.3 which are all polynomials:

$$E_0 : H_{j-5/2}, H_{j-3/2}, H_{j-1/2}, E_1 : H_{j-3/2}, H_{j-1/2}, H_{j+1/2},$$

$$\text{and} \quad E_2 : H_{j-1/2}, H_{j+1/2}, F_{j+3/2} \tag{2.21}$$

Note that:

$$H_{j-1/2} = \sum_{i=0}^{j-1} F_i \Delta x \tag{2.22}$$

Compact schemes are used for these three candidates:

$$E_0 : \; a_0 H'_{j-3/2} + H'_{j-1/2} = (-b_0 H_{j-5/2} - a_0 H_{j-3/2} + c_0 H_{j-1/2}) / \Delta x$$

$$E_1 : \; a_1 H'_{j-3/2} + H'_{j-1/2} + a_1 H'_{j+1/2} = a_1 (H_{j+1/2} - H_{j-3/2}) / \Delta x \tag{2.23}$$

$$E_2 : \; H'_{j-1/2} + a_2 H'_{j+1/2} = (b_2 H_{j+3/2} + a_2 H_{j+1/2} - c_2 H_{j-1/2}) / \Delta x$$

For high order, we pick

$$a_0 = 2, a_1 = \frac{1}{4}, a_2 = 2, a_0 = 2, a_1 = \frac{3}{4}, a_2 = 2, b_0 = \frac{1}{2}, b_2 = \frac{1}{2}, c_0 = \frac{5}{2}, c_2 = \frac{5}{2} \tag{2.24}$$

E_0 and E_2 have third order, but E_1 has fourth order of accuracy.

The compact scheme for each candidate is:

$$E_0 : \; 2H'_{j-3/2} + H'_{j-1/2} = \left(-\frac{1}{2} H_{j-5/2} - 2H_{j-3/2} + \frac{5}{2} H_{j-1/2} \right) \Big/ h = \frac{5}{2} F_{j-1} + \frac{1}{2} F_{j-2}$$

$$E_1 : \frac{1}{4} H'_{j-3/2} + H'_{j-1/2} + \frac{1}{4} H'_{j+1/2} = \frac{3\left(H_{j+1/2} - H_{j-3/2}\right)}{4h} = \frac{3}{4}(F_j + F_{j-1}) \tag{2.25}$$

$$E_2:\ H'_{j-1/2}+2H'_{j+1/2}=\left(\frac{1}{2}H_{j+3/2}+2H_{j+1/2}-\frac{5}{2}H_{j-1/2}\right)\Big/h=\frac{1}{2}F_{j+1}+\frac{5}{2}F_j$$

3) Non-bias compact scheme

Let $E=C_0E_0+C_1E_1+C_2E_2$ and $C_0=\frac{1}{18}, C_1=\frac{16}{18}, C_2=\frac{1}{18}$

$$\text{E:}\frac{1}{3}H'_{j-3/2}+H'_{j-1/2}+\frac{1}{3}H'_{j+1/2}=\frac{1}{36}F_{j-2}+\frac{29}{36}F_{j-1}+\frac{29}{36}F_j+\frac{1}{36}F_{j+1} \tag{2.26}$$

Similarly, E at point $j+1/2$ is

$$\frac{1}{3}H'_{j-1/2}+H'_{j+1/2}+\frac{1}{3}H'_{j+3/2}=\frac{1}{36}F_{j-1}+\frac{29}{36}F_j+\frac{29}{36}F_{j+1}+\frac{1}{36}F_{j+2} \tag{2.27}$$

Subtracting the previous equation at point j-1/2, we get

$$\frac{1}{3}F'_{j-1}+F'_j+\frac{1}{3}F'_{j+1}=\frac{1}{h}(-\frac{1}{36}F_{j-2}-\frac{7}{9}F_{j-1}+\frac{7}{9}F_{j+1}+\frac{1}{36}F_{j+2}) \tag{2.28}$$

This is a standard sixth order compact scheme. The stencil candidates are $E_0: F_{j-2}, F_{j-1}$, $E_1: F_{j-1}, F_j$, and $E_2: F_j, F_{j+1}$ for $H'_{j-1/2}=\hat{F}_{j-1/2}$. This also shows the WCS uses smaller candidate stencils but gets higher accuracy comparing with the 5th order WENO.

The procedure described above implies that a sixth order centered compact scheme can be constructed by a combination of three lower order schemes. In order to achieve the non-oscillatory property, the WENO weights (Jiang et al., 1996) are introduced to determine new weights for each stencil. The weights are determined

according to the smoothness of the function on each stencil. Following the WENO method, the new weights are defined as

$$w_k = \frac{g_k}{\sum_{i=0}^{2} g_i} \qquad g_k = \frac{C_k}{(e + IS_k)^p} \tag{2.29}$$

where e is a small positive number to prevent the denominator becoming zero and p is a parameter to control the weighting. Actually, the weights are very sensitive to p. We set p as a function of smoothness instead of constant. When p=0, the 6th order standard compact scheme is recovered. IS_k is a smoothness measurement which is defined in (2.16). Through the Taylor expansion, it can be easily proved that in smooth regions the new weights w_k satisfy:

$$w_k = C_k + O(h^2) \text{ and}$$

$$w_2 - w_0 = O(h^3) \tag{2.30}$$

The new scheme is formed using these new weights:

$$E = w_0 E_0 + w_1 E_1 + w_2 E_2 \tag{2.31}$$

The leading error of E is a combination of the leading errors of the original schemes, which is:

$$(\frac{1}{12} w_0 - \frac{1}{12} w_2) f^{(4)} h^3 + (-\frac{1}{15} w_0 + \frac{1}{120} w_1 - \frac{1}{15} w_2) f^{(5)} h^4 \tag{2.32}$$

When equation (2.30) is satisfied, the leading error of the new scheme can be written as $O(h^6)$ and the new scheme remains its 6th order of accuracy.

2.4 Uniform weighted compact / non-compact schemes

Now, we try to use one parameter a -family of the compact scheme. On each stencil, a compact difference scheme is derived as follows by matching the coefficients in Taylor series to obtain corresponding orders.

$$
\begin{aligned}
&S_0 : F_0 \qquad a_0^- f'_{i-1} + f'_i = \frac{1}{h}\left[b_0^- f_{i-2} + a_0^- f_{i-1} + c_0 f_i\right] \\
&S_1 : F_1 \qquad a_1^- f'_{i-1} + f'_i + a_1^+ f'_{i+1} = \frac{1}{h}\left[a_1^- f_{i-1} + c_1 f_i + a_1^+ f_{i+1}\right] \\
&S_2 : F_2 \qquad f'_i + a_2^+ f'_{i+1} = \frac{1}{h}\left[c_2 f_i + a_2^+ f_{i+1} + b_2^+ f_{i+2}\right]
\end{aligned}
\tag{2.19}
$$

The linear weight for each stencil is C_0, C_1, C_2, respectively. Then we have 16 unknowns,

$$
\begin{aligned}
&C_0, \quad a_0^-, \quad b_0^-, \quad a_0^-, \quad c_0, \\
&C_1, \quad a_1^-, \quad a_1^+, \quad a_1^-, \quad a_1^+, \quad c_1, \\
&C_2, \quad a_2^+, \quad a_2^+, \quad b_2^+, \quad c_2,
\end{aligned}
$$

For each stencil, a compact scheme of lower order is established. By matching the coefficients in Taylor's series, we have the following conditions:

$$
c_0 = \frac{3 + a_0^-}{2}, \quad c_1 = 0, \quad c_2 = -\frac{3 + a_0^-}{2}, \quad a_2^+ = 2, \quad a_0^- = -2,
$$

$$
b_0^- = \frac{1 - a_0^-}{2}, \quad b_2^+ = -\frac{1 - a_0^-}{2},
$$

$$
a_1^- = \frac{a_1^+ - 3a_1^- - 1}{2}, \quad a_1^+ = -\frac{a_1^+ - 3a_1^- - 1}{2}
\tag{2.20}
$$

In order to reassemble the standard compact scheme in equation (2.10), we have the following conditions:

$$C_0 a_0^- + C_1 a_1^- = a\ , \quad C_0 + C_1 + C_2 = 1, \quad C_1 a_1^+ + C_2 a_2^+ = a\ ,$$

$$C_0 b_0^- = -\frac{1}{12}(4a - 1), \quad C_0 a_0^- + C_1 a_1^- = -\frac{1}{3}(a + 2),$$

$$C_0 c_0 + C_1 c_1 + C_2 c_2 = 0, \quad C_1 a_1^+ + C_2 a_2^+ = \frac{1}{3}(a + 2),$$

$$C_2 b_2^- = \frac{1}{12}(4a - 1) \tag{2.21}$$

where a is treated as a parameter.

All these nonlinear equations above are not independent to each other. Therefore, the system is not closed for 16 unknowns. We can add an artificial condition to close the system. Note that this is a non-linear system. Let us try to use $a_1^+ = \frac{3a}{4}$ artificially. We have a closed system with the following solution listed in Table 2.1

Table 2.1 Coefficients for the compact scheme on each stencil S0, S1, S2 ($a_1^+ = \frac{3a}{4}$)

	C	a_-	a_+	b_-	a_-	c	a_+	b_+
S_0	$\frac{5a-2}{6(3a-2)}$	$\frac{6a(2a-1)}{5a-2}$		$\frac{1}{2}-\frac{3a(2a-1)}{5a-2}$	-2	$\frac{3}{2}+\frac{3a(2a-1)}{5a-2}$		
S_1	$\frac{4(a-1)}{3(3a-2)}$	$\frac{3a}{4}$	$\frac{3a}{4}$		$-\frac{3a}{4}-\frac{1}{2}$	0	$\frac{3a}{4}+\frac{1}{2}$	
S_2	$\frac{5a-2}{6(3a-2)}$		$\frac{6a(2a-1)}{5a-2}$			$-\frac{3}{2}-\frac{3a(2a-1)}{5a-2}$	2	$-\frac{1}{2}+\frac{3a(2a-1)}{5a-2}$

Every coefficient varies smoothly and monotonically when a varies from 0 to 1/3. Therefore, the scheme is formulated as follows,

$$S_0 : F_0 \qquad \frac{6a(2a-1)}{5a-2} f'_{j-1} + f'_j = \frac{1}{h}\left[\left(\frac{1}{2} - \frac{3a(2a-1)}{5a-2}\right) f_{j-2} - 2 f_{j-1} + \left(\frac{3}{2} + \frac{3a(2a-1)}{5a-2}\right) f_j\right]$$

$$S_1 : F_1 \qquad \frac{3a}{4} f'_{j-1} + f'_j + \frac{3a}{4} f'_{j+1} = \frac{1}{h}\left[-\left(\frac{3a}{4} + \frac{1}{2}\right) f_{j-1} + \left(\frac{3a}{4} + \frac{1}{2}\right) f_{j+1}\right]$$

$$S_2 : F_2 \qquad f'_j + \frac{6a(2a-1)}{5a-2} f'_{j+1} = \frac{1}{h}\left[-\left(\frac{3}{2} + \frac{3a(2a-1)}{5a-2}\right) f_j + 2 f_{j+1} - \left(\frac{1}{2} - \frac{3a(2a-1)}{5a-2}\right) f_{j+2}\right]$$

For candidates S_0 and S_2, the function values at three grid points and first derivative at one grid point are used to calculate f'_j. Thus the scheme is at least second-order accurate (third-order if $a = 1/3$) and one sided. For candidate S_1, the function values at two grid points and first derivative at two grid points are used to calculate f'_j. Thus the scheme is at least second-order accurate (fourth-order if $a = 1/3$) and centered. Then a specific weight is assigned to each equation, and a new scheme is obtained by a summation of the equations.

$$F = C_0 F_0 + C_1 F_1 + C_2 F_2 \tag{2.23}$$

where $C_0 + C_1 + C_2 = 1$. By choosing the weights in table 1, the scheme reproduces the standard compact scheme:

$$a f'_{i-1} + f'_i + a f'_{i+1} = \left(-\frac{1}{12}(4a-1) f_{i-2} - \frac{1}{3}(a+2) f_{i-1} + \frac{1}{3}(a+2) f_{i+1} + \frac{1}{12}(4a-1) f_{i+2}\right)/h + t_i \tag{2.24}$$

which has sixth-order of accuracy if we pick $a = 1/3$, but fourth-order if we pick $a \neq 1/3$. As we discussed in section 2.3.2, we use WENO weights, w_0, w_1, w_2 instead of C_0, C_1, C_2.

Following the WENO method, the weights are defined as:

$$w_k = \frac{g_k}{\sum_{i=0}^{2} g_i}, \quad g_k = \frac{C_k}{(e + IS_k)^p},$$

$$C_0 = \frac{5a-2}{6(3a-2)}, C_1 = \frac{4(a-1)}{3(3a-2)}, C_2 = \frac{5a-2}{6(3a-2)},$$

where e is a small number to prevent the denominator becoming zero. p is an important parameter to control weights. IS_k is the smoothness measurements which are defined in section 2.2.2.

The final scheme is $F = w_0 F_0 + w_1 F_1 + w_2 F_2$:

$$[w_0 \frac{6a(2a-1)}{5a-2} + w_1 \frac{3a}{4}] f'_{j-1} + f'_j + [w_1 \frac{3a}{4} + w_2 \frac{6a(2a-1)}{5a-2}] f'_{j+1} =$$
$$\{w_0 [\frac{1}{2} - \frac{3a(2a-1)}{5a-2}] f_{j-2} - [2w_0 + w_1 (\frac{3a}{4} + \frac{1}{2})] f_{j-1} + (w_0 - w_2)[\frac{3}{2} + \frac{3a(2a-1)}{5a-2}] f_j$$
$$+ [2w_2 + w_1 (\frac{3a}{4} + \frac{1}{2})] f_{j+1} - w_2 [\frac{1}{2} - \frac{3a(2a-1)}{5a-2}] f_{j+2} \} / h$$

(2.25)

Note that there is only one parameter a which has not been determined yet.

2.5 Determination of parameter *a*

Apparently, determination of a becomes the central stage of our research. Instead of using fixed a, we determine the value of a according to the smoothness of

the function. All the other coefficients become the functions of a . In this work, we first define a as

$$a = \frac{1}{3} - \left[\left(\overline{IS_0} - \frac{1}{3} \right)^2 + \left(\overline{IS_1} - \frac{1}{3} \right)^2 + \left(\overline{IS_2} - \frac{1}{3} \right)^2 \right]^{\frac{1}{2}} / 2 \tag{2.26}$$

where $\overline{IS_k} = \dfrac{IS_k + e}{\sum_{i=0}^{2} (IS_k + e)}$,

again e is a small positive number. In smooth regions, the three normalized smoothness are nearly equal, namely, $\overline{IS_0} = \overline{IS_1} = \overline{IS_2} = \dfrac{1}{3}$. Then a equals to 1/3 and the 6th order standard compact scheme recovered. We achieve global dependency and the best resolution. In shock regions, for instance, the worst case gives us dramatically different weights. After normalization we have $\overline{IS_0} = 1, \overline{IS_1} = \overline{IS_2} = 0$. Then $a = 0$ and we achieve the local dependency and non-oscillatory property from the weighting procedure.

However, these kinds of WENO weights based on differences of left hand side, central, right hand side smoothness would not distinguish the low and high frequency waves and will give same a for both low frequency and high frequency waves. It may mislead to give $a = 1/3$ for center point of the shock if we capture the shock with more than three grid points. Apparently, we need to consider the fourth measurement of the smoothness, IS_{ave} which is high for high frequency and low for low frequency. In this work, we define a in the following way:

$$a_{final} = \min \{ a (1 - a_1 * IS_{ave}) * a_2, \frac{1}{3} \} \quad (2.27)$$

We also define a function called smoothness which will control the compact and non-compact switch and everything:

Smoothness = 1.0-3.0* a or a = (1.0-smoothness)/3.0

When smoothness = 1.0 where is discontinuous, a =0.0 and non-compact scheme will be used. When smoothness=0.0, a =1/3 and the standard 6th order compact scheme will be recovered.

2.6 Recovery to 8th order accuracy in smooth areas

In smooth area, the scheme will become a standard 6th order compact scheme and keep 6th order in accuracy:

$$\frac{1}{3} f'_{j-1} + f'_j + \frac{1}{3} f'_{j+1} = \frac{1}{h}(-\frac{1}{36} f_{j-2} - \frac{7}{9} f_{j-1} + \frac{7}{9} f_{j+1} + \frac{1}{36} f_{j+2}) \quad (2.28)$$

Using 5 grid points, we can also get an 8th order scheme by following scheme:

$$\frac{1}{36} f'_{j-2} + \frac{4}{9} f'_{j-1} + f'_j + \frac{4}{9} f'_{j+1} + \frac{1}{36} f'_{j+2} = \frac{1}{h}(-\frac{25}{216} f_{j-2} - \frac{40}{54} f_{j-1} + \frac{40}{54} f_{j+1} + \frac{25}{216} f_{j+2}) \quad (2.29)$$

Subtracting (2.29) by (2.28), we get the residual:

$$F_3: \frac{1}{36} f'_{j-2} + \frac{1}{9} f'_{j-1} + \frac{1}{9} f'_{j+1} + \frac{1}{36} f'_{j+2} = \frac{1}{h}(-\frac{19}{216} f_{j-2} + \frac{1}{27} f_{j-1} - \frac{1}{27} f_{j+1} + \frac{19}{216} f_{j+2}) \tag{2.30}$$

The final finite difference scheme can be written as

$$F = w_0 F_0 + w_1 F_1 + w_2 F_2 + w_3 F_3 \tag{2.31}$$

Where

$$w_3 = 3.0 * a = 1.0 - Smoothness \tag{2.32}$$

which is 1 in the smooth area and becomes zero near the shock or other discontinuities. In this way, the accuracy will be recovered to 8th order by 5-point stencil in the smooth area. Of course, a penta-diagonal system has to be solved on each grid line.

The above derivation is based on the six order compact scheme:

$$F_6 = w_0 F_0 + w_1 F_1 + w_2 F_2 + O(h^6) \tag{2.33}$$

In order to get 8th order accuracy in the smooth area, we can use:

$$F = (1-w_3)[w_0 F_0 + w_1 F_1 + w_2 F_2] + w_3 F_8 + (1-w_3) k_6 h^6 + w_3 k_8 h^8 \tag{2.34}$$

where F_8 is a standard 8th order compact scheme with 5 grid points. In the smooth area, $w_3 = 1.0$, we obtain 8th order of accuracy.

Here, we use the 6th order WCS as our base scheme. However, this method is universal and we can use for any base scheme. For example, we can use 5th order WENO as our base scheme or use the uniform weighted compact and non-compact

scheme (UWCNC) as our base scheme. The basic idea is to get 8th order of accuracy recovered in the smooth area, but bias near the shock to avoid numerical oscillations.

The remained question is how to detect shock correctly and accurately and then chose a right switch function or sharply weighted function, w_3, based on the smoothness, which has been discussed much in previous sections.

CHAPTER 3

APPLICATION OF UWCNC TO 1-D PROBLEMS

3.1 One-dimensional linear wave equation

The scheme is tested by solving a linear wave equation with a smooth initial function:

$$u_t + u_x = 0\,,\ u(x,0) = \sin(2px) \text{ where } 0 \le x \le 1\,. \tag{3.1}$$

The calculation stops at $t = 0.3$ and the errors are listed in table 3.1. The computation shows the 6th order accuracy is achieved.

Table 3.1 Errors and Order of Accuracy

N	L_1 Error	L_1 Order	L_2 Error	L_2 Order	L_∞ Error	L_∞ Order
8	1.06E02	-	3.67E03	-	2.05E02	-
16	8.66E05	6.93	2.46E05	7.22	2.00E04	6.68
32	1.37E06	5.98	2.94E07	6.39	4.37E06	5.51
64	2.23E08	5.93	3.74E09	6.30	1.11E07	5.30
128	3.45E10	6.01	4.95E11	6.24	2.86E09	5.27
256	4.49E12	6.26	5.73E13	6.43	5.98E11	5.58

We also test both UWCNC and WENO schemes on a 1-D linear wave equation with jump initial function:

$$u_t + u_x = 0\,,\quad u(x,0) = \begin{cases} 1.0 & \textit{if} \quad 0.1 \le x \le 0.4 \\ 0.5 & \textit{otherwise} \end{cases}$$

The calculation stops at $t = 0.3$ and the solutions are illustrated in Figure 3.1. The results indicate that standard compact scheme is not suitable for shocks while both UWCNC and WENO schemes work. Furthermore, UWCNC has less dissipation than WENO near shocks which means a sharper transition is obtained. Figure 3.2 shows the numerical solution of linear wave equation with high frequency sinuous function as initial condition. Traditional 6^{th} order compact scheme has the best resolution, while UWCNC-6 has similar behaviors and very small dissipation. WENO-5 is the most dissipative.

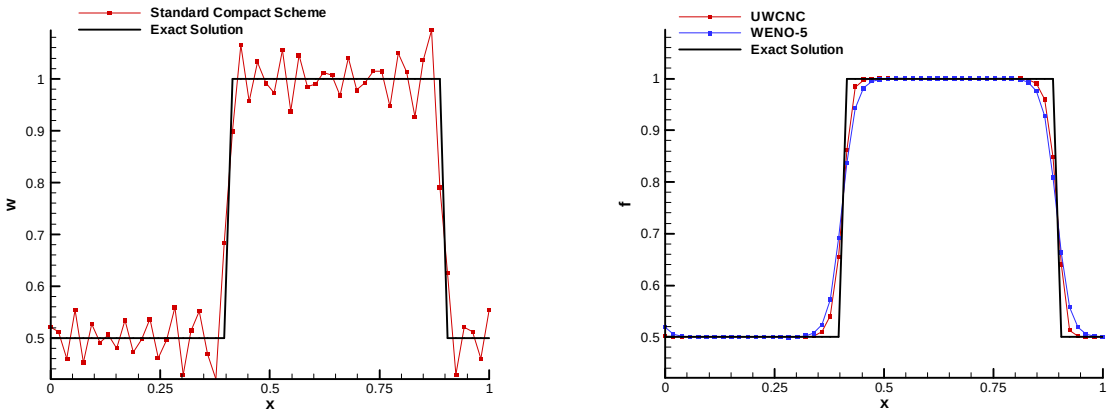

Figure 3.1 Numerical test over linear wave equation: square wave function.

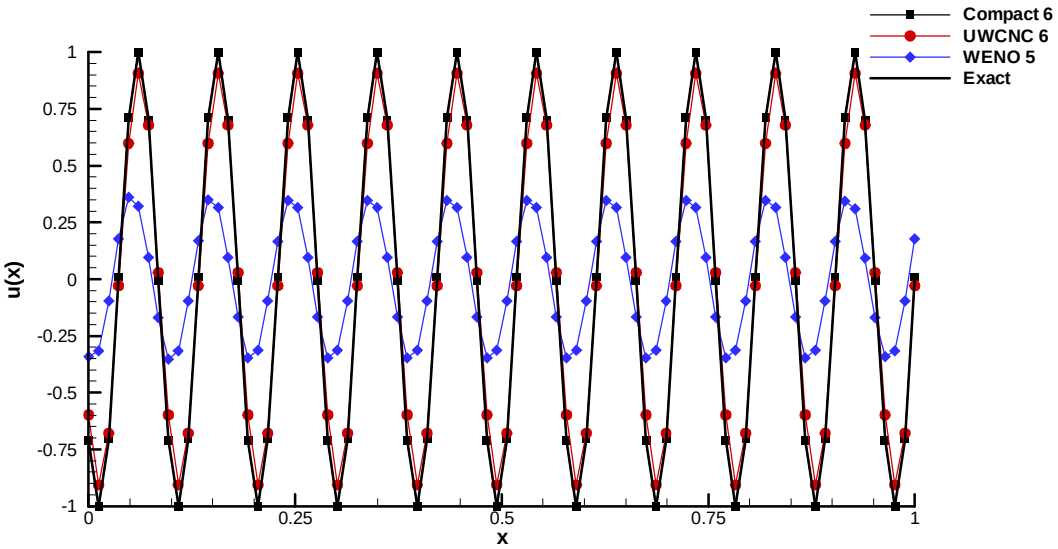

Figure 3.2 Numerical test over linear wave equation: High frequency sinuous function.

3.2 One-dimensional Euler equations

The governing conservation law for one-dimensional inviscid fluid flow can be formulated as follows,

$$r_t + (ru)_x = 0$$
$$(ru)_t + (ru^2 + p)_x = 0$$
$$E_t + [u(E+p)]_x = 0$$

These are the conservation of mass, momentum and energy, respectively. They can also be expressed in a very compact notation by defining a column vector $\boldsymbol{U}$ of conserved variables and flux vectors $\boldsymbol{F(U)}$.

$$U_t + F(U)_x = 0$$

where

$$U = \begin{bmatrix} r \\ ru \\ E \end{bmatrix}, \quad F = \begin{bmatrix} ru \\ ru^2 + p \\ u(E+p) \end{bmatrix}.$$

3.2.1 Shock tube flow (Sod's problem)

One classic benchmark is the Sod's test problem which sets up a shock tube with quiescent gas on both left- and right-hand side. The initial condition is set as

$$(r, u, p) = \begin{cases} (1, 0, 1), & x < 0; \\ (0.125, 0, 0.1) & x \geq 0. \end{cases}$$

The solution consists of a left-traveling rarefaction wave, a contact surface and a right-traveling shock wave.

To solve the Euler equations, a three-step TVD Runge-Kutta is used in time marching and Steger-Warming flux vector splitting is used and the derivatives of splitting flux F^+, F^- are calculated using our new scheme. In this case, a is defined as in Equation 2.27. The distributions of velocity u and pressure are shown in Figure 3.3. Comparisons are also made with the solutions obtained using 5th order WENO scheme. From Figure 3.4, it can be found the UWCNC scheme (referred to as LJX) captured the shock sharper and smeared the expansion wave and shock less then the 5th order WENO. Figure 3.7 shows a locally enlarged comparison between UWCNC, WENO, and WENO with 1600 grid points which we consider as an exact solution. Figure 3.8 show the smoothness measured by our definition which is the only parameter to control

the compact and non-compact scheme switch. The figure shows the shock is well captured with smoothness=1.0 ($a = 0$) and the smoothness measured on the coarser grid (N=100) and finer grid (N=200) are pretty consistent.

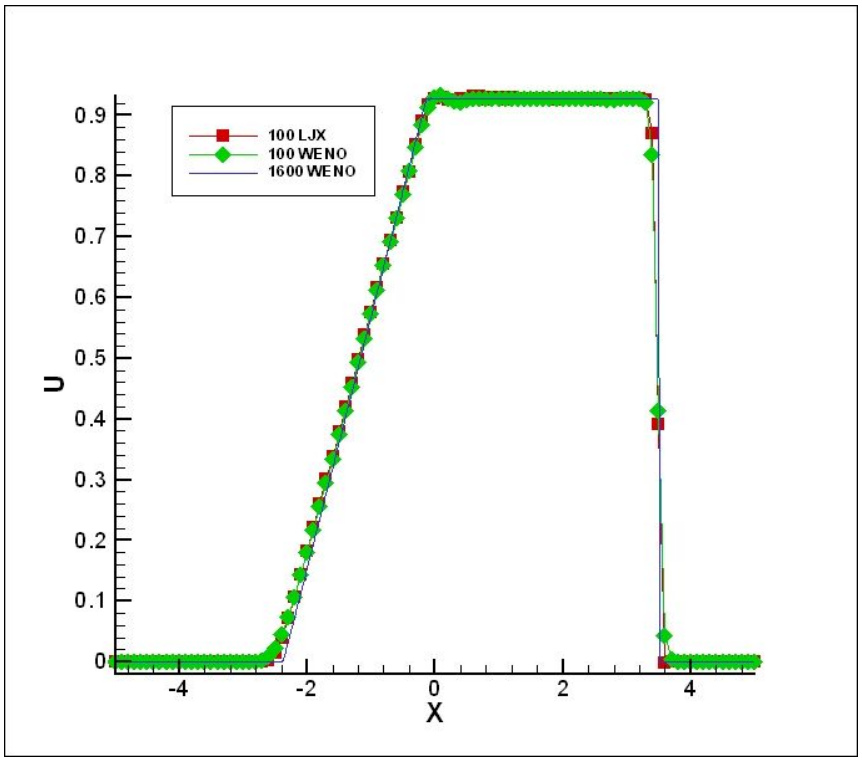

Figure 3.3 Numerical test for 1D shock-tube problem, t=2, N=100
Velocity Distribution

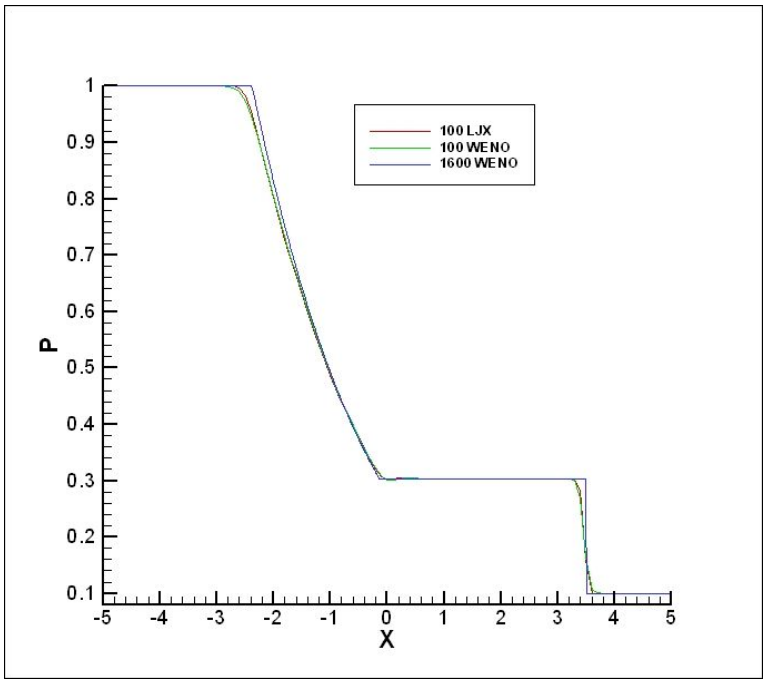

Figure 3.4 Numerical test for 1D shock-tube problem, t=2, N=100
Pressure Distribution

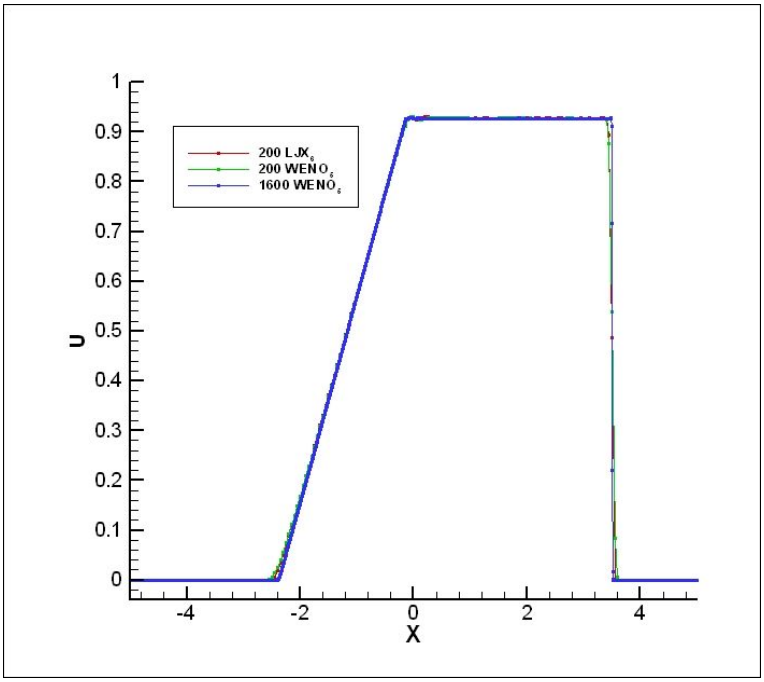

Figure 3.5 Numerical test for 1D shock-tube problem, t=2, N=200
Velocity Distribution

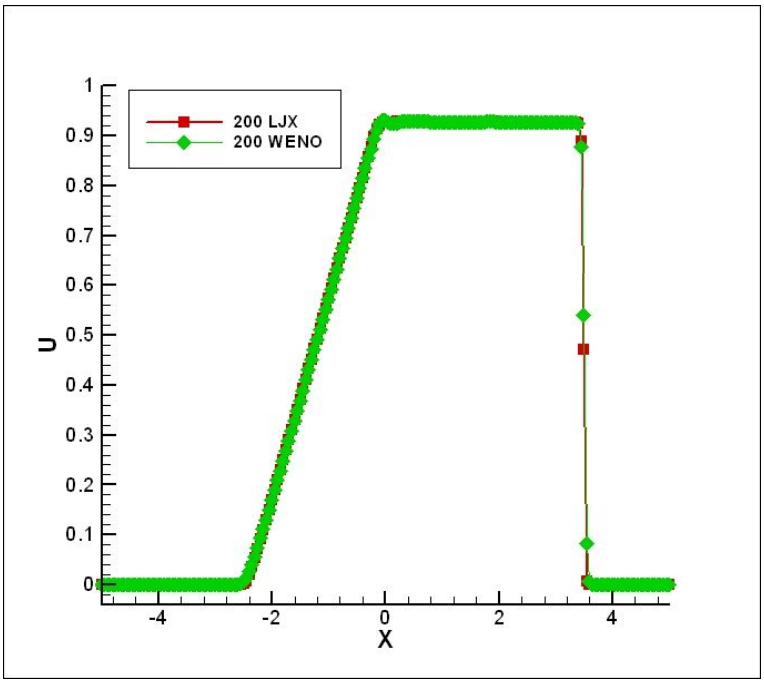

Figure 3.6 Numerical test for 1D shock-tube problem, t=2, N=200
Comparison of Velocities

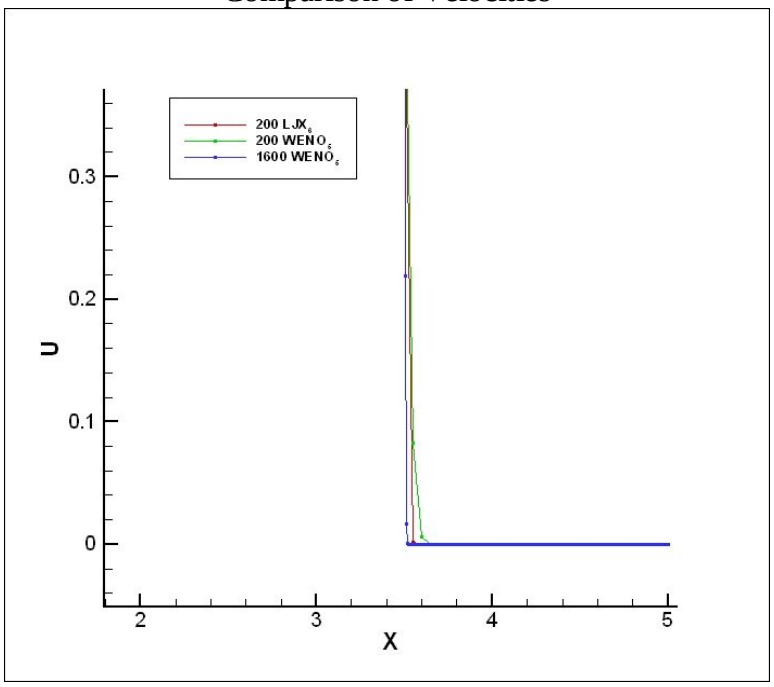

Figure 3.7 Numerical test for 1D shock-tube problem, t=2, N=200
Comparison of Velocities, locally enlarged

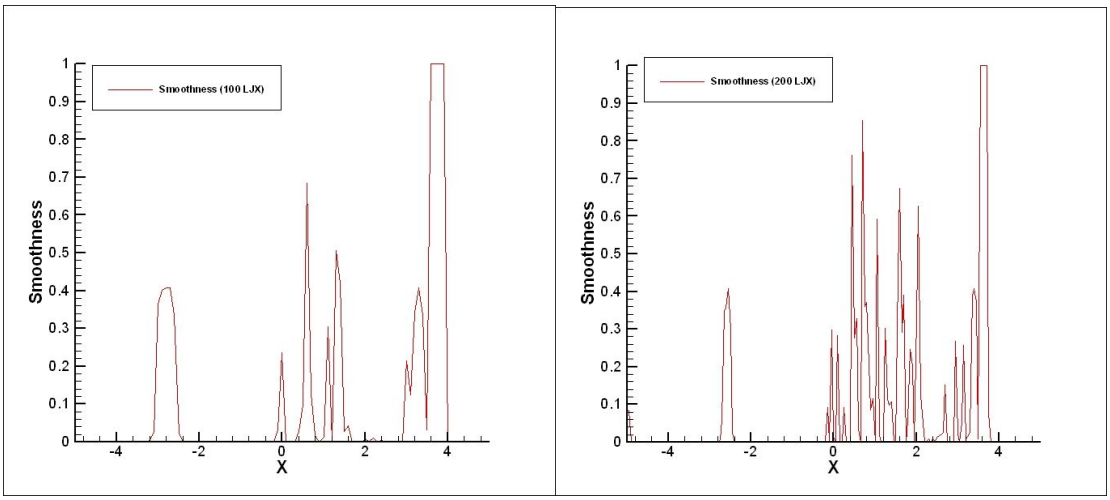

Figure 3.8 Smoothness for 1D shock-tube problem, t=2, N=100 and 200

3.2.2 Shock-entropy interaction

To test the capability of the new scheme in both shock capturing and resolution, we applied it to the 1-D problem of shock/entropy wave interaction. In this case, Euler equations (3.3) are solved with the following initial conditions:

$$(r, u, p)_0 = \begin{cases} (3.857143, 2.629369, 10.33333), & x < -4; \\ (1 + 0.2\sin(5x), 0, 1) & x \geq -4. \end{cases} \tag{3.5}$$

a is calculated using (2.27). Figures 3.9 – 3.17 show the solutions of the density distribution on the coarser and finer grids. On the coarser grid with grid number of N=200, our new scheme shows much better resolution for small length scales than the 5th order WENO (Figures 3.9 – 3.13). Apparently, there is an order difference in resolution between our 6th order UWCNC scheme and the 5th order scheme. This is because UWCNC uses central, non-dissipative, compact scheme with weights in the

shock area and recovers high order compact away from the shock. The numerical results by our UWCNC scheme with 200 grid points are even comparable with the 5th order WENO scheme with 1600 grid points. On the finer grid (N=400), both the 6th order UWCNC and 5th order WENO schemes show a good resolution (Figure 3.14 – 3.17). However, we can still find our 6th order UWCNC scheme has a much better resolution for the fifth wave left from the shock (Figure 3.11). In addition, the UWCNC captures the shock in a much sharper way for all shocks. On the shocks developed by the sinuous waves, only one grid point was found on the shock (Figure 3.15 and 3.17). Again, Figures 3.18 – 3.20 show the smoothness measured by our definition which is the only parameter to control the compact and non-compact scheme switch. The figure shows the main shock is well captured with smoothness=1.0 ($a = 0$) and the shocks developed by the sine function are also well captured. The smoothness measured on the coarser grid (N=200 and 400) and finer grid (N=1600) are quite consistent.

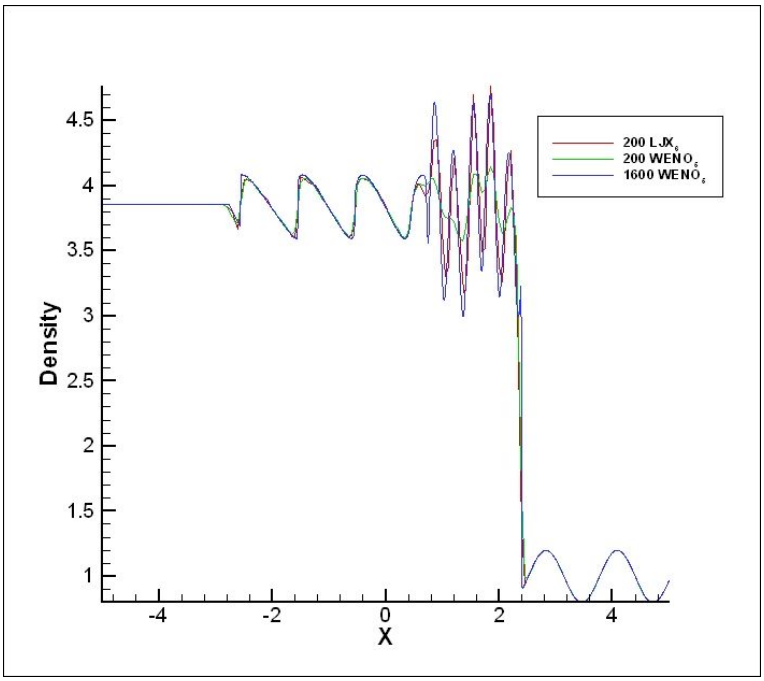

Figure 3.9 Numerical test for 1D shock-entropy wave interaction problem, t=1.8 – Density Distribution, N=200

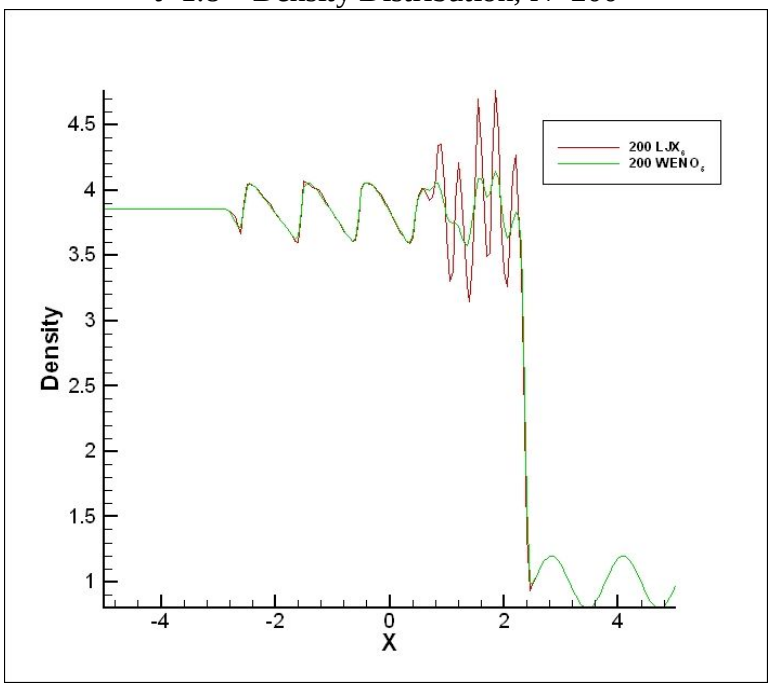

Figure 3.10 Numerical test for 1D shock-entropy wave interaction problem, t=1.8, N=200 – Comparison of Density Distributions

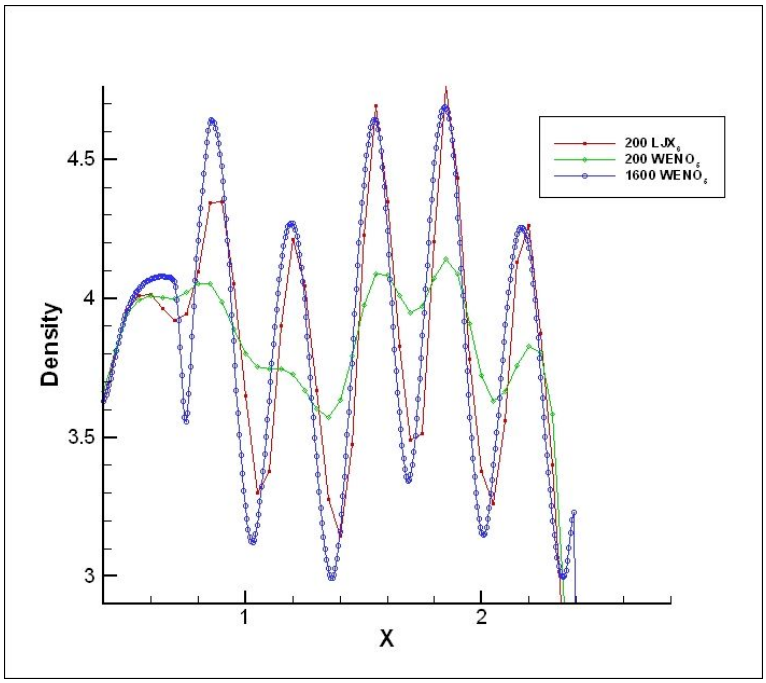

Figure 3.11 Numerical test for 1D shock-entropy wave interaction problem, t=1.8, N=200 – Comparison of Density Distributions, locally enlarged

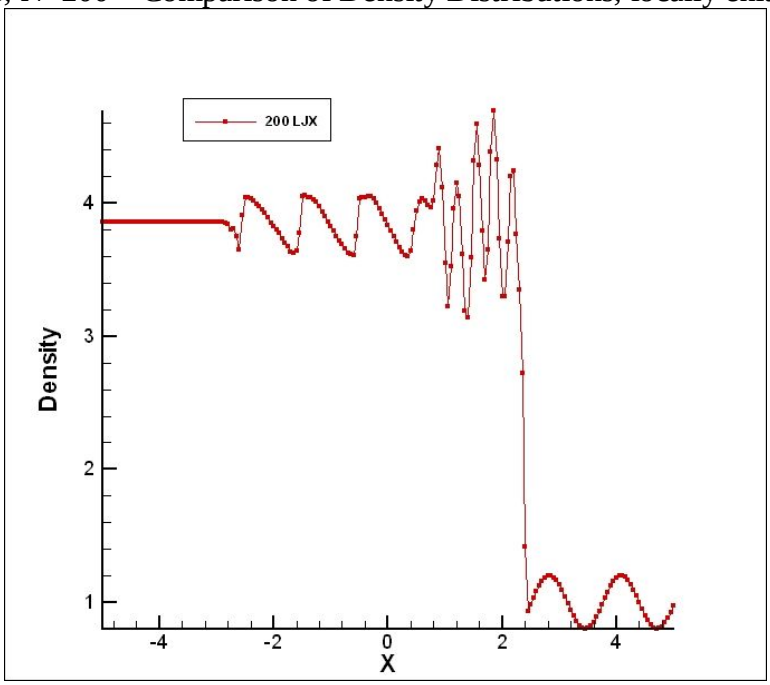

Figure 3.12 Numerical test for 1D shock-entropy wave interaction problem, t=1.8 – Density distribution, UWCNC, N=200

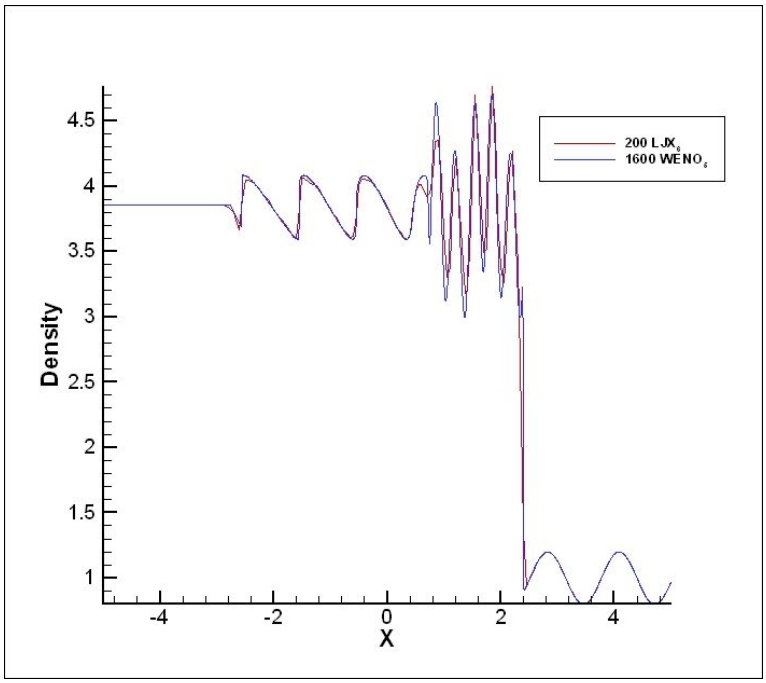

Figure 3.13 Numerical test for 1D shock-entropy wave interaction problem, t=1.8 – Comparison of UWCNC N=200 with WENO N=1600

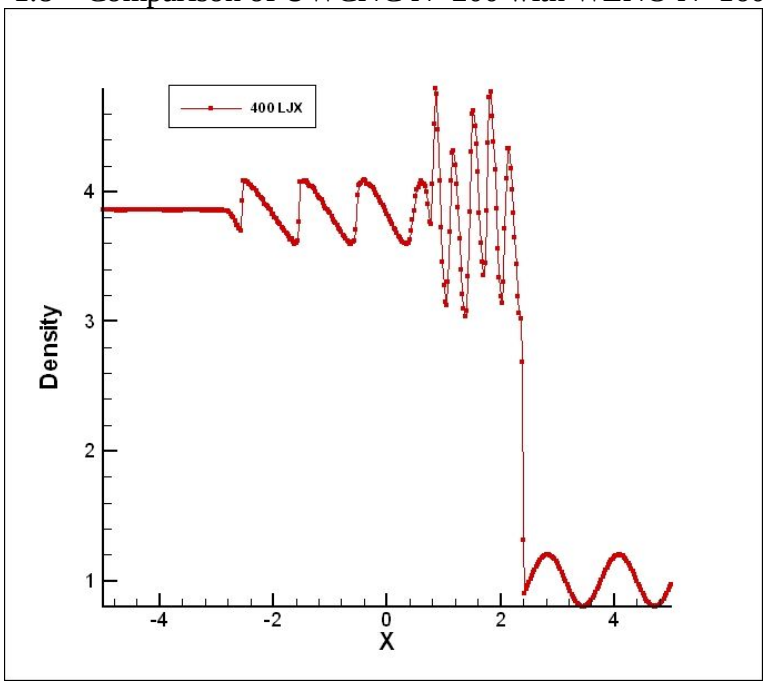

Figure 3.14 Numerical test for 1D shock-entropy wave interaction problem, t=1.8, N=400 – UWCNC-6

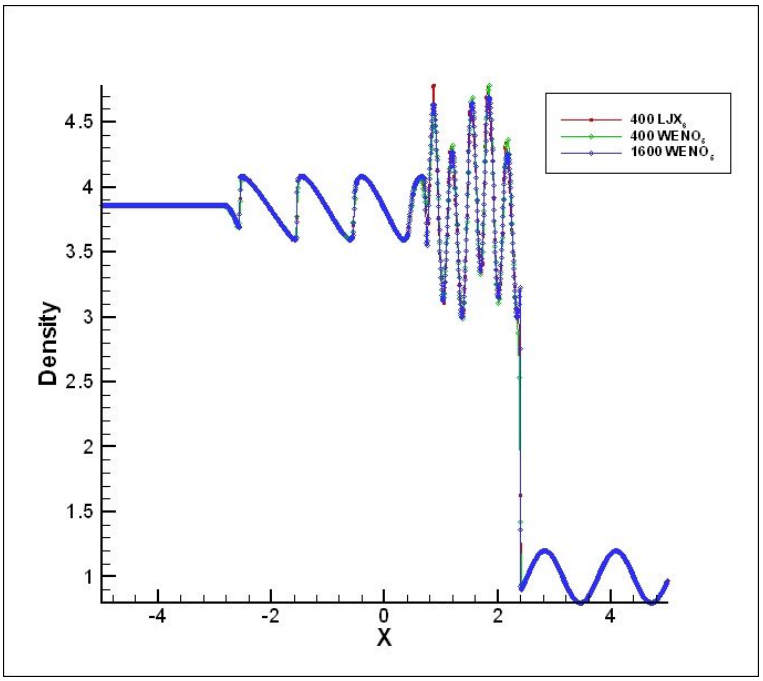

Figure 3.15 Numerical test for 1D shock-entropy wave interaction problem, t=1.8, N=400 – Comparison of WENO-5 and UWCNC-6

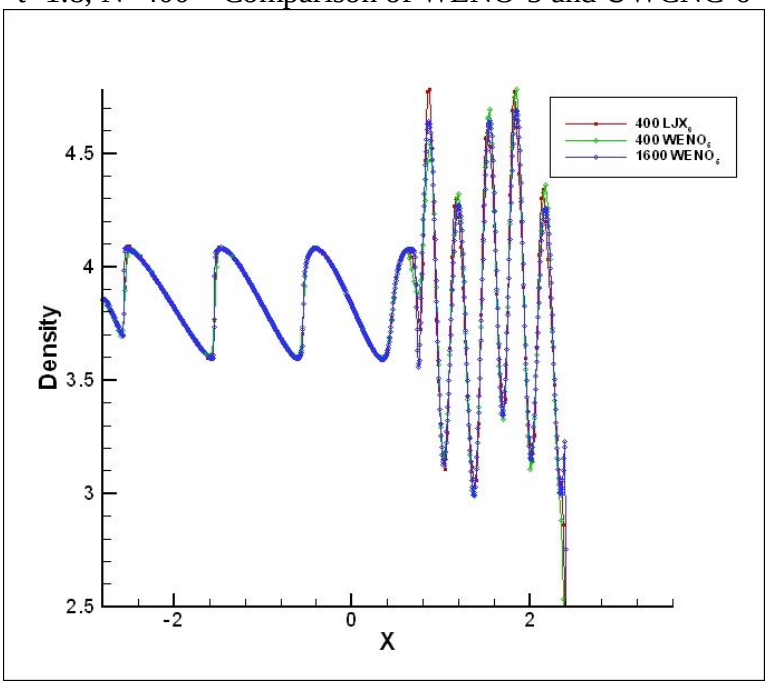

Figure 3.16 Numerical test for 1D shock-entropy wave interaction problem, t=1.8, N=400 – Comparison of WENO-5 and UWCNC-6 (locally enlarged)

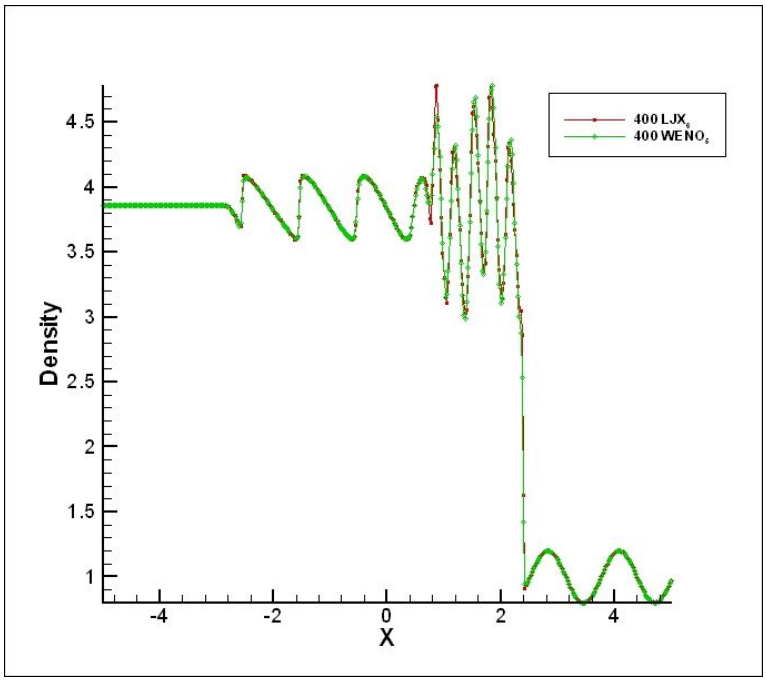

Figure 3.17 Numerical test for 1D shock-entropy wave interaction problem, t=1.8, N=400 – Comparison of WENO-5 and UWCNC-6

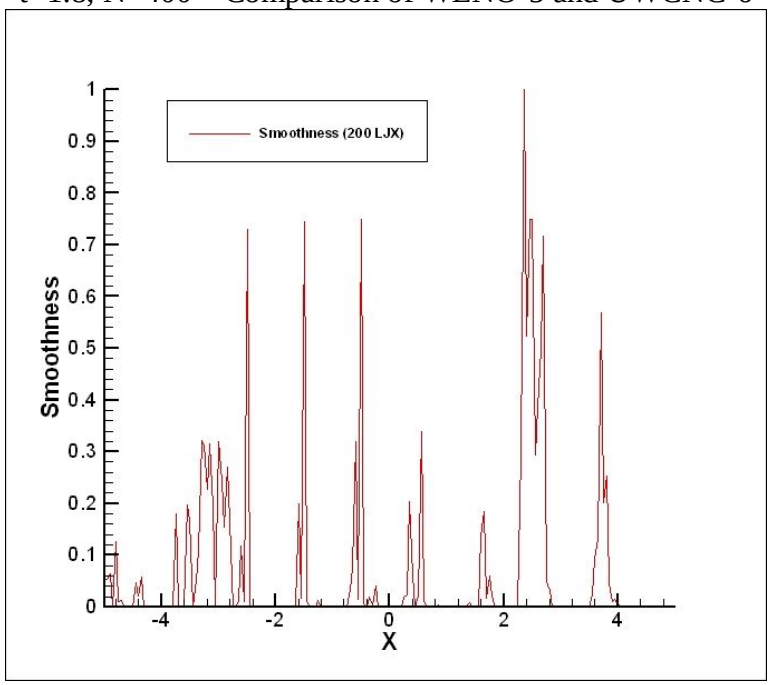

Figure 3.18 Smoothness for 1D shock-entropy problem, t=2, N=200

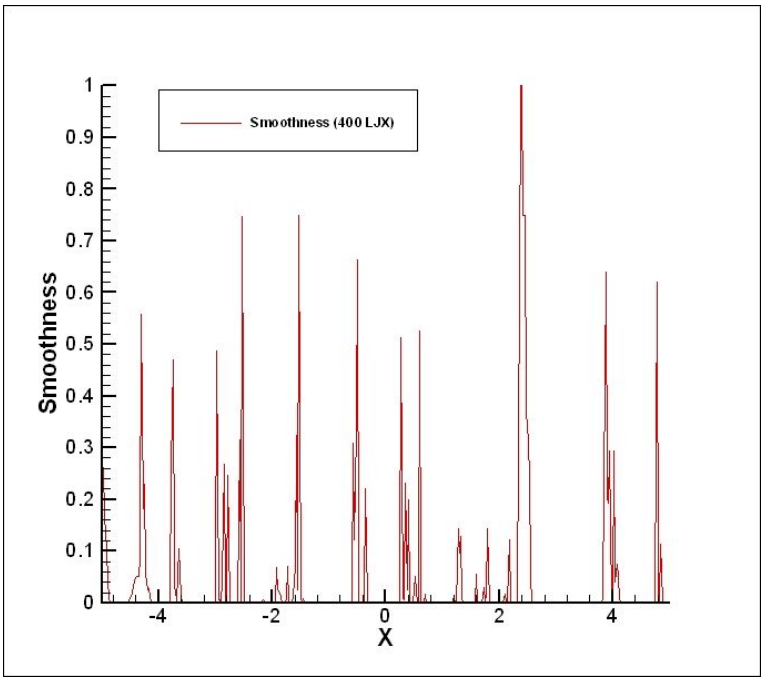

Figure 3.19 Smoothness for 1D shock-entropy problem, t=2, N=400

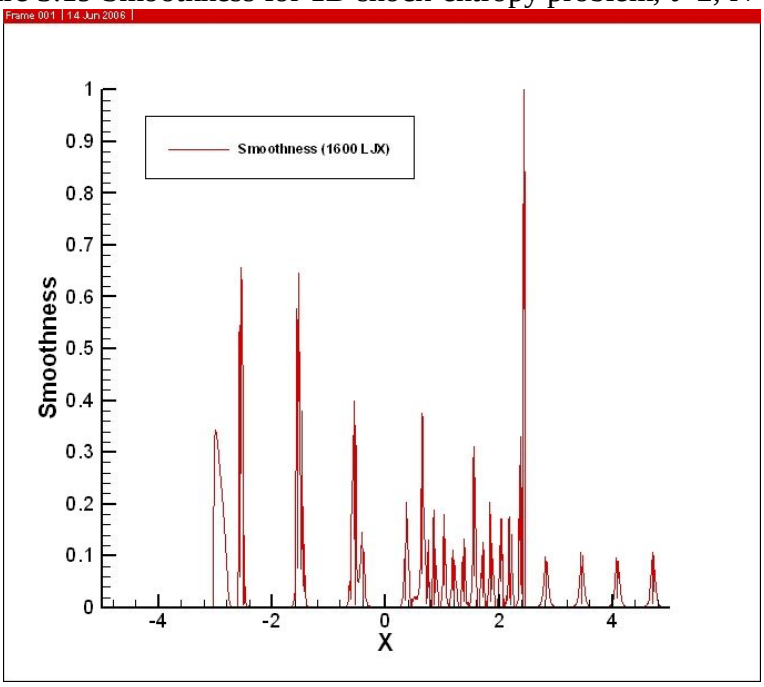

Figure 3.20 Smoothness for 1D shock-entropy problem, t=2, N=1600

CHAPTER 4

APPLICATION OF UWCNC TO 2-D EULER EQUATIONS

4.1 Two-dimensional Euler equations

The conservative form of the 2-D Euler Equations is as follows,

$$U_t + F(U)_x + G(U)_y = 0$$

where

$$U = \begin{bmatrix} r \\ ru \\ rv \\ E \end{bmatrix}, \quad F = \begin{bmatrix} ru \\ ru^2 + p \\ ruv \\ u(E+p) \end{bmatrix} \quad G = \begin{bmatrix} rv \\ ruv \\ rv^2 + p \\ v(E+p) \end{bmatrix}.$$

4.2 Incident shock reflection

A simple uniform grid is generated for 2-D incident shock reflection.

Computational domain: $0<x<1.95$, $0<y<0.588$

Boundary Condition:

Inflow Mach Number $M_\infty=3.0$

Flow Deflection Angle 15^o

The results are plotted and compared as follows,

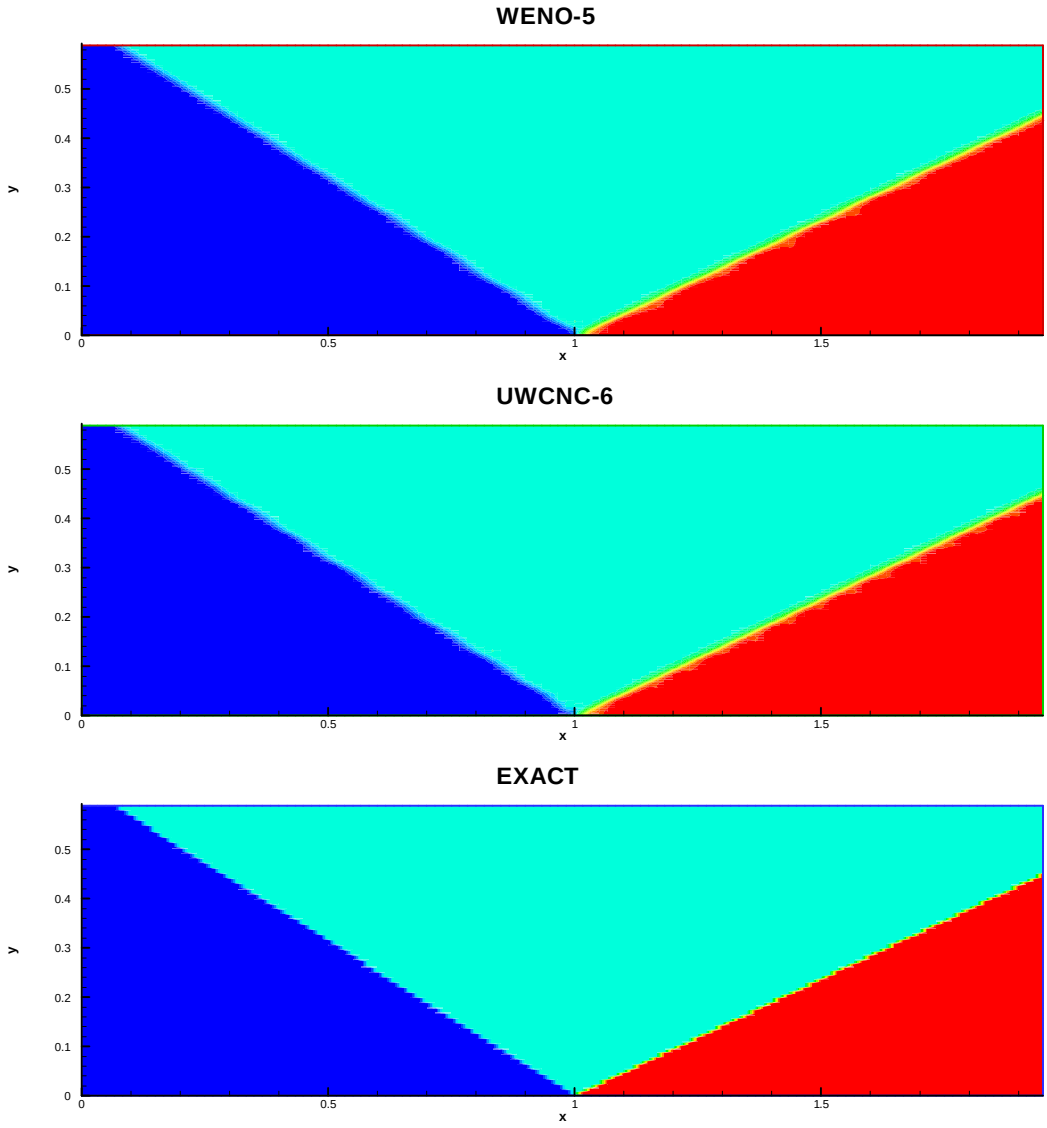

Figure 4.1 Pressure Contours of Incident Shock Reflection.
Comparison of Numerical Solutions With Exact Solution.

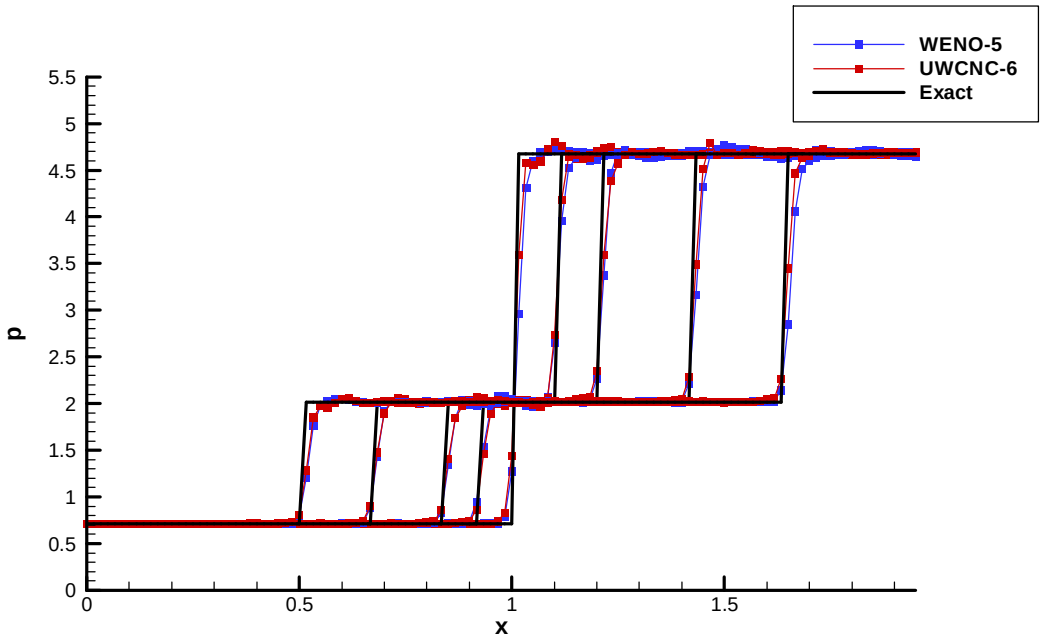

Figure 4.2 Pressure profiles at y=0, y=0.052, y=0.104, y=0.208, y=0.311

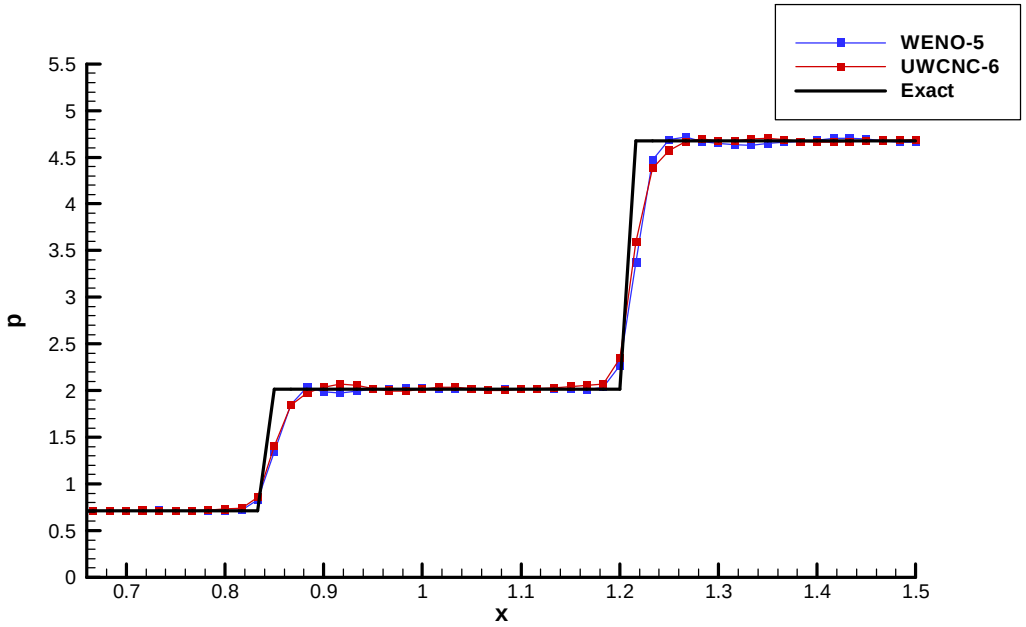

Figure 4.3 Detailed pressure distribution at y=0.104

The results show that UWCNC has slightly sharper shocks than WENO, but the difference is not significant. The UWCNC-6 scheme captures shock captures shock as good as (or a little better than) WENO-5 scheme does.

4.3 Cylindrical shock tube problem

To further test the shock capturing ability of UWCNC in two dimensions, cylindrical shock tube problem is solved in a square domain.

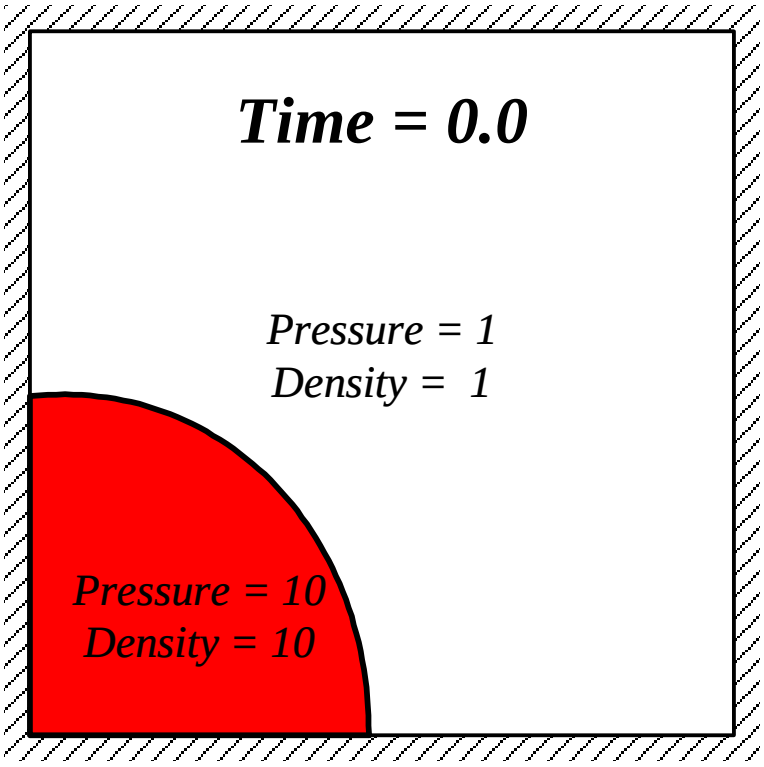

Figure 4.4 Cylindrical Shock Tube Problem: Geometry and Initial Conditions

Initial conditions are specified as follows,

For $x^2+y^2<0.5$: $P = 10$ and $r = 10$

Elsewhere: $P = 1$ and $r = 1$

$u = v = 0$

The 2-D Euler equations are solved in this domain with adiabatic and reflective wall boundaries. A simple uniform grid is generated for 2-D cylindrical shock tube problem. The flow pattern is as follows,

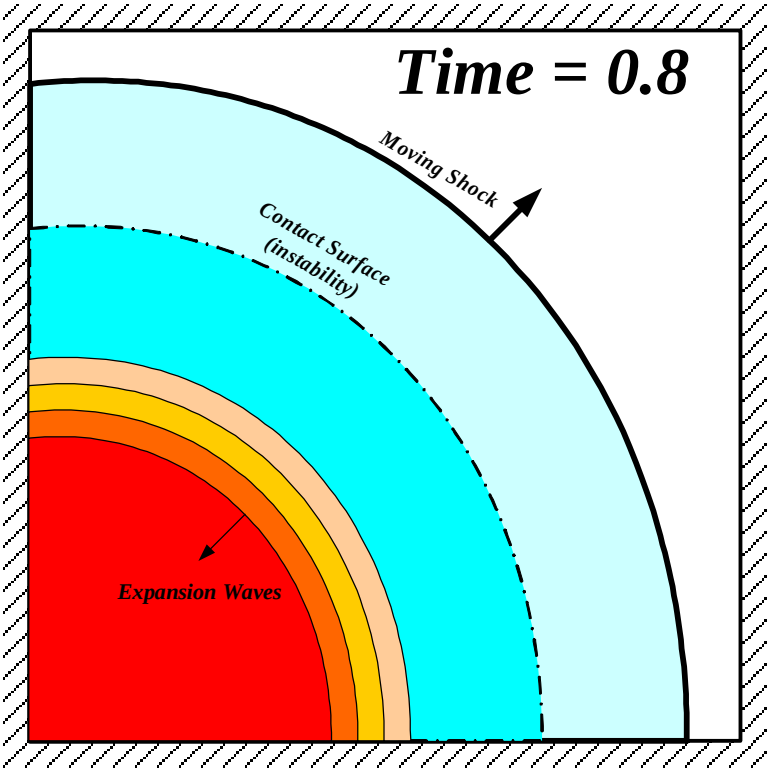

Figure 4.5 Flow pattern of cylindrical shock tube problem.

The contact surface is unstable and sensitive to small perturbations in this test case. Therefore, there are small structures on the contact surface. 2-D Euler equation is solved over two grid levels, 81x81 and 161x161. The results are the following.

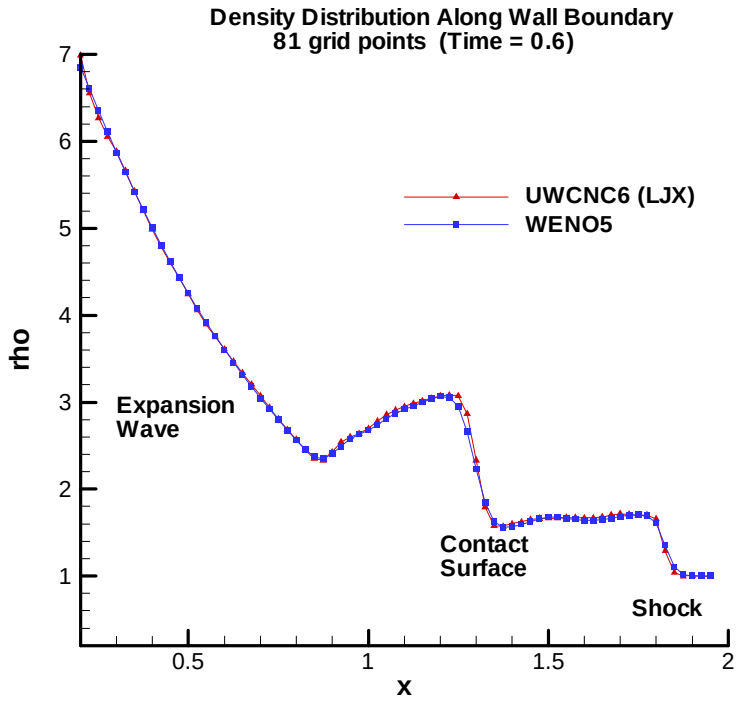

Figure 4.6 Density distribution along wall surface (radial). Grids: 81x81

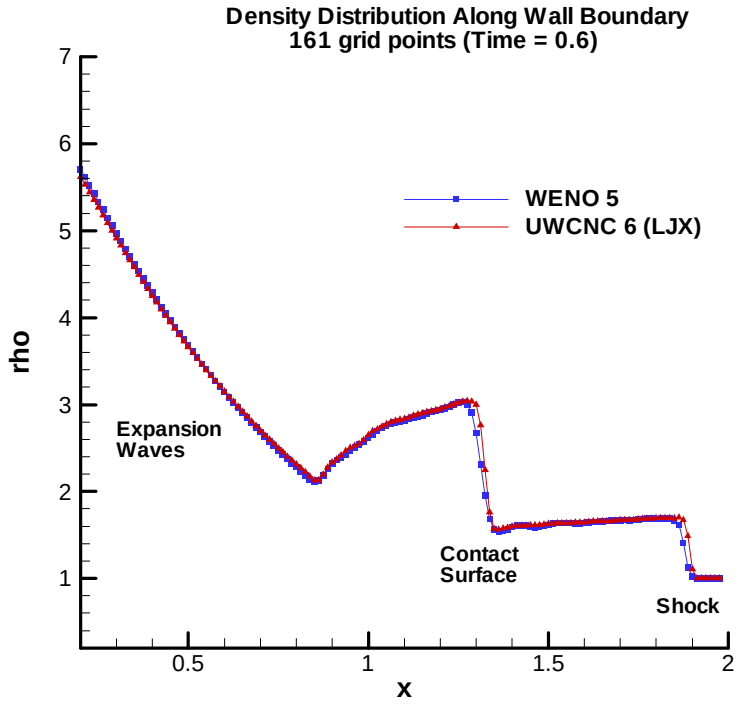

Figure 4.7 Density distribution along wall surface (radial). Grids: 161x161

The results show again that UWCNC-6 has captures shock and contact surfaces sharper than WENO-5.

However, in both cases the flows are inviscid which makes the solution relatively simple. To further test the capability of resolving small structures, the Navier-Stokes Equations are solved. Corresponding comparisons are also made between UWCNC-6 and WENO-5.

CHAPTER 5

APPLICATION OF UWCNC TO 2-D NAVIER-STOKES EQUATIONS

5.1 Two-dimensional Navier-Stokes equations

The 2-D Navier-Stokes Equations can also be written in conservative form. Furthermore, the equations are written in general curvilinear coordinates as follows,

$$\frac{1}{J}\frac{\partial Q}{\partial t}+\frac{\partial(F-F_v)}{\partial x}+\frac{\partial(G-G_v)}{\partial h}=0$$

where

$$Q=\begin{bmatrix} r \\ ru \\ rv \\ E \end{bmatrix},\quad F=\frac{1}{J}\begin{bmatrix} rU \\ rUu+px_x \\ rUv+px_y \\ U(E+p) \end{bmatrix},\quad G=\frac{1}{J}\begin{bmatrix} rV \\ rVu+ph_x \\ rVv+ph_y \\ V(E+p) \end{bmatrix},$$

$$F_v=\frac{1}{J}\begin{bmatrix} 0 \\ t_{xx}x_x+t_{yx}x_y \\ t_{xy}x_x+t_{yy}x_y \\ q_x x_x+q_y x_y \end{bmatrix},\quad G_v=\frac{1}{J}\begin{bmatrix} 0 \\ t_{xx}h_x+t_{yx}h_y \\ t_{xy}h_x+t_{yy}h_y \\ q_x h_x+q_y h_y \end{bmatrix}.$$

and $J=\dfrac{\partial(x,h)}{\partial(x,y)}$ is Jacobian of the coordinate transformation between curvilinear (x,h) and Cartesian (x,y) frames, and x_x, x_y, h_x, h_y are coordinate transformation metrics. The contravariant velocity component U, V are defined as

$$U=ux_x+vx_y \quad , \quad V=uh_x+vh_y$$

E denotes the total energy,

$$E = \frac{p}{g-1} + \frac{1}{2} r\left(u^2 + v^2\right)$$

The components of the viscous stress tensor and heat flux are denoted by t_{xx}, t_{xy}, t_{xx} and q_x, q_y, respectively.

5.2 Shock / laminar boundary layer interaction : case 1

5.2.1 Inflow profile generation

It has been shown that the resolution of the flow at the leading edge is critical for the boundary layer. In order to resolve both the boundary layer and shock waves efficiently, the flow around leading edge is computed separately by using the same code. A uniform flow field is used as initial condition in the region far away from the adiabatic wall. For the inflow boundary (including both left and upper boundary), parameters are fixed to the given values as follows,

$$M_\infty = 3.0, \quad \mathrm{Re} = 3\times10^5, \quad \mathrm{Pr} = 0.7$$

Where M_∞ is the inflow Mach number, ***Re*** and ***Pr*** are the Reynolds number and Prandtl number, respectively. At wall surface, adiabatic and non-slip boundary condition is employed. Non-reflection boundary condition is used at outflow boundary to avoid non-physical reflections. The flow converged to a steady solution.

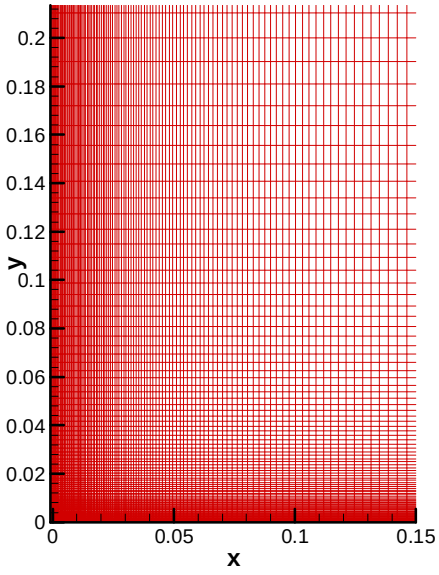

Figure 5.1 Numerical results of inflow generator – Grids

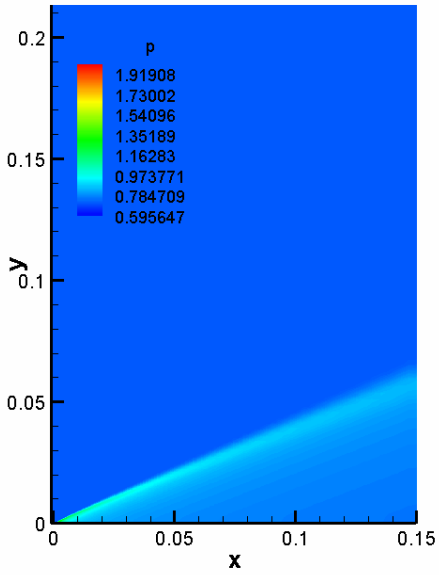

Figure 5.2 Numerical results of inflow generator – Pressure

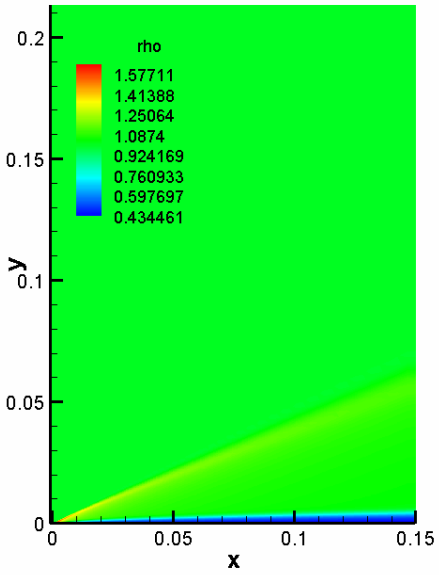

Figure 5.3 Numerical results of inflow generator – Density

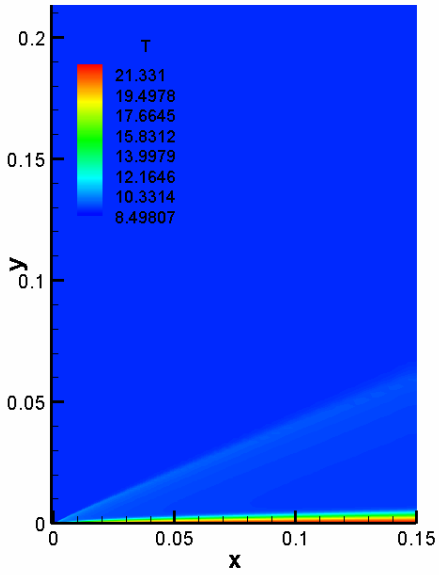

Figure 5.4 Numerical results of inflow generator – Temperature

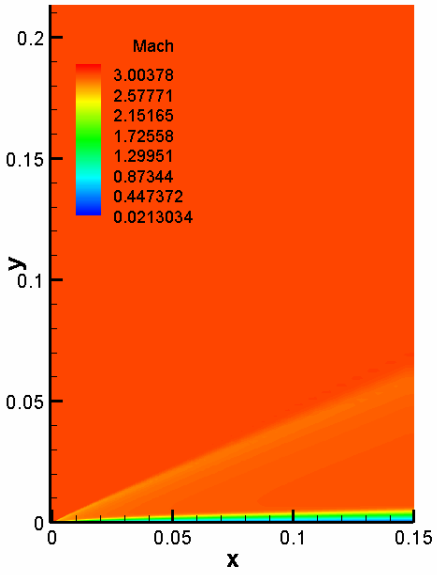

Figure 5.5 Numerical results of inflow generator – Mach Number

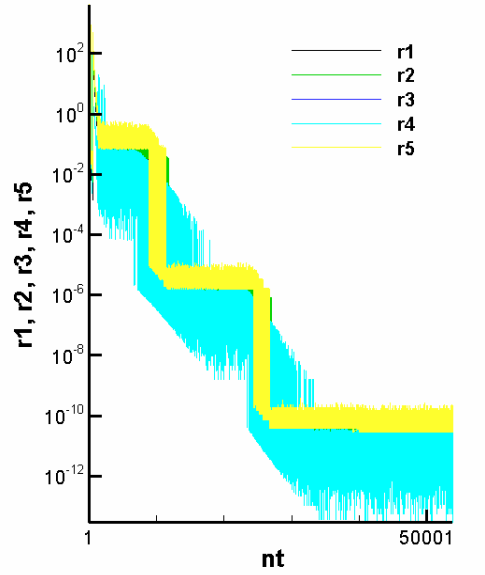

Figure 5.6 Numerical results of inflow generator – Convergence History

5.2.2 Main flow solver

5.2.2.1 Numerical grid generation

In order to resolve the small structures inside boundary layer, the grid is stretched vertically as shown below.

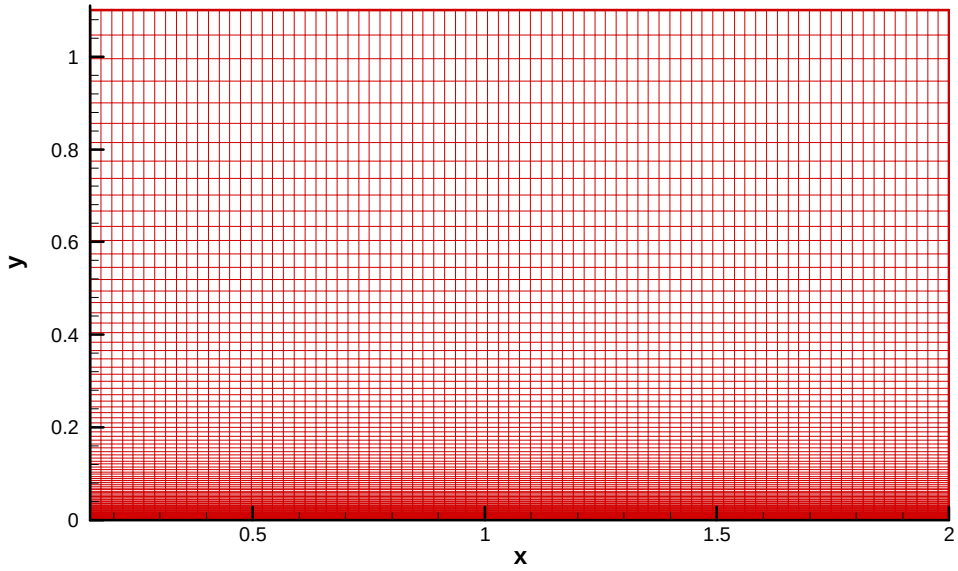

Figure 5.7 Numerical grids for main flow solver of shock / boundary layer interaction

5.2.2.2 Initial and boundary conditions

The inflow boundary is given by the profile of the previous inflow generator. The oblique shock is given such that the flow deflection angle is ten degrees. At wall surface, adiabatic and non-slip boundary condition is employed. Non-reflection boundary condition is used at outflow boundary to avoid non-physical reflections.

5.2.2.3 Numerical results

The numerical results are shown below. For better illustration, the graphs of vorticities are vertically stretched by a factor of 3.

(i) Fine Grids (241x141)

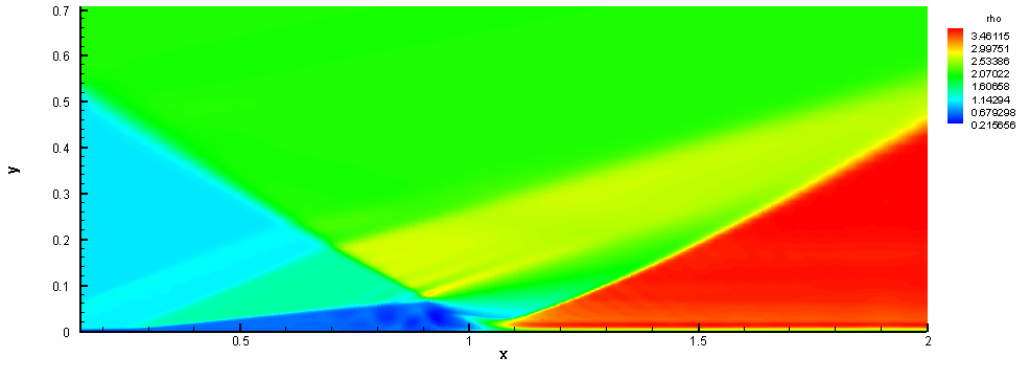

Figure 5.8 Numerical Results of WENO-5 over Fine Grids (241x141) – Density Contours

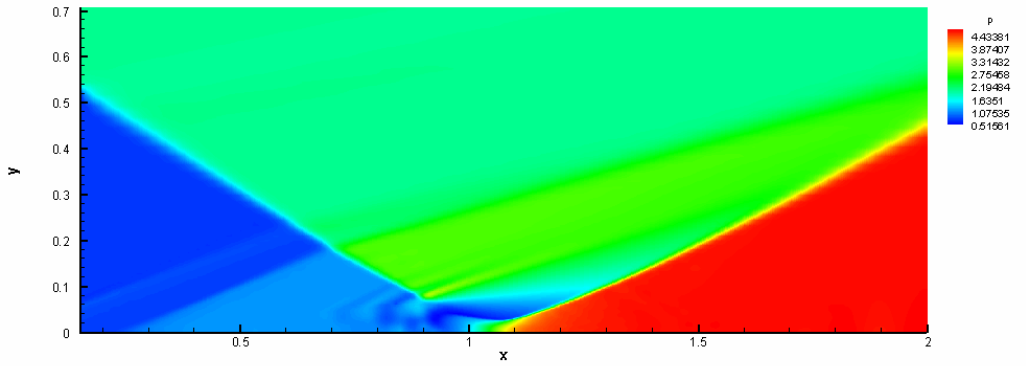

Figure 5.9 Numerical Results of WENO-5 over Fine Grids (241x141) – Pressure Contours

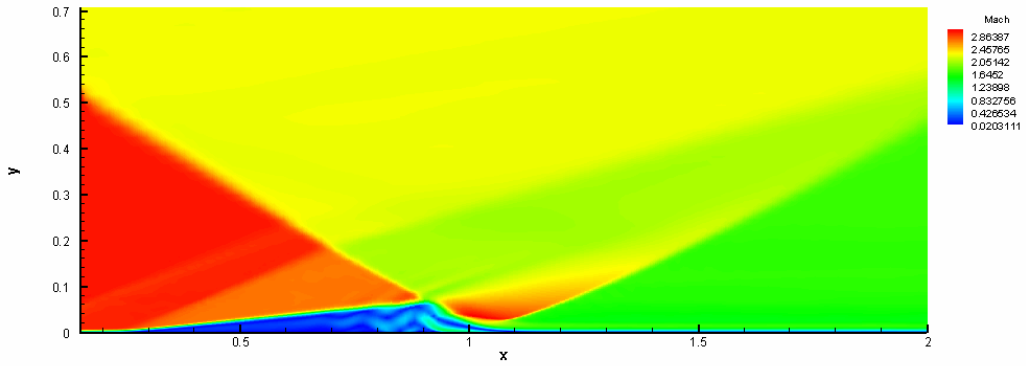

Figure 5.10 Numerical Results of WENO-5 over Fine Grids (241x141) – Mach Number

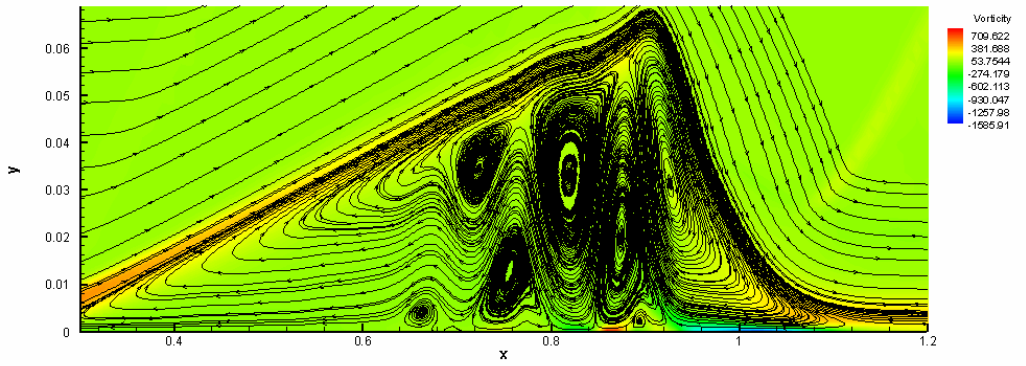

Figure 5.11 Numerical Results of WENO-5 over Fine Grids (241x141) – Vorticity and Stream Trace

(ii) Coarse Grids (121x141) UWCNC-6

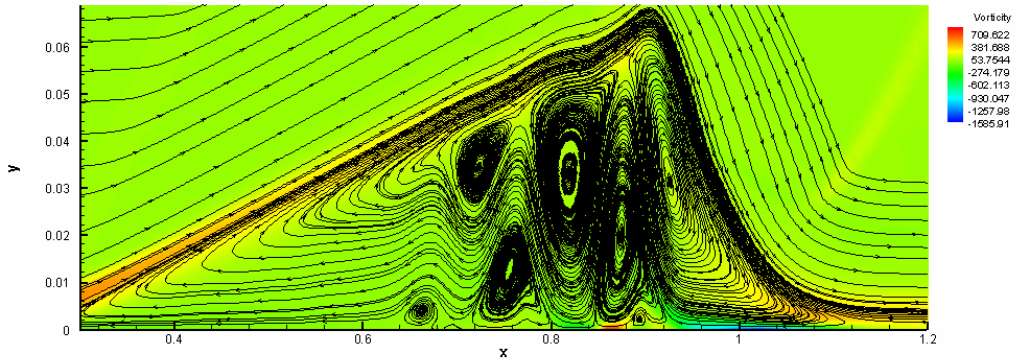

Figure 5.12 Vorticity and Stream Trace (121x141) UWCNC-6

(iii) Coarse Grids (121x141) WENO-5

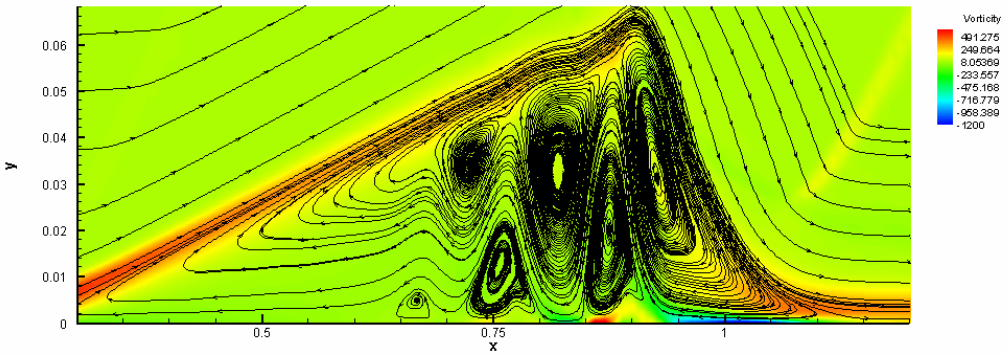

Figure 5.13 Vorticity and Stream Trace (121x141) WENO-5

5.3 Shock / laminar boundary layer interaction: case 2

In this test case, the Reynolds number is 10^5 and the inflow Mach number is set to 2.15. The overall pressure ratio is 1.55. For comparison, the inflow condition was set as same investigated by Degrez et al (1987). Their experimental work has shown the shock-boundary layer interaction is laminar and two-dimensional. Therefore, we can do a 2-D numerical simulation and compare with their computational and experimental results. The computational grids is 257x257 (Figure 5.14). The grid stretching in stremwise direction is 1.01. The stretching in wall normal direction is 1.015. The same 2-D Navier-Stokes equation is solved as the governing equation.

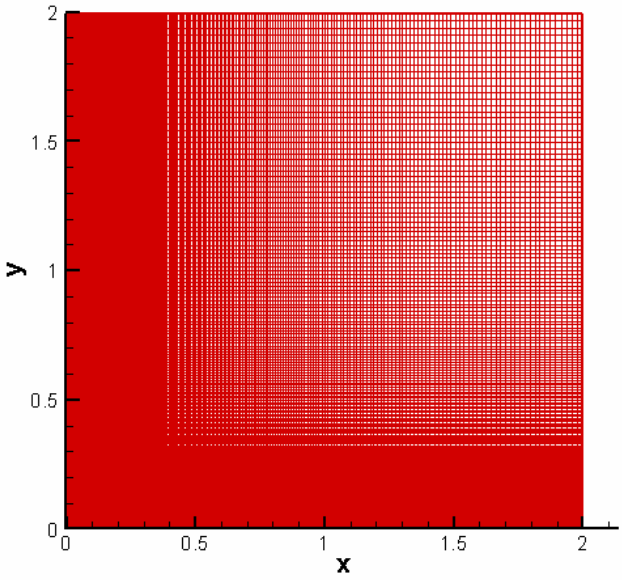

Figure 5.14 Computational Grids (257x257)

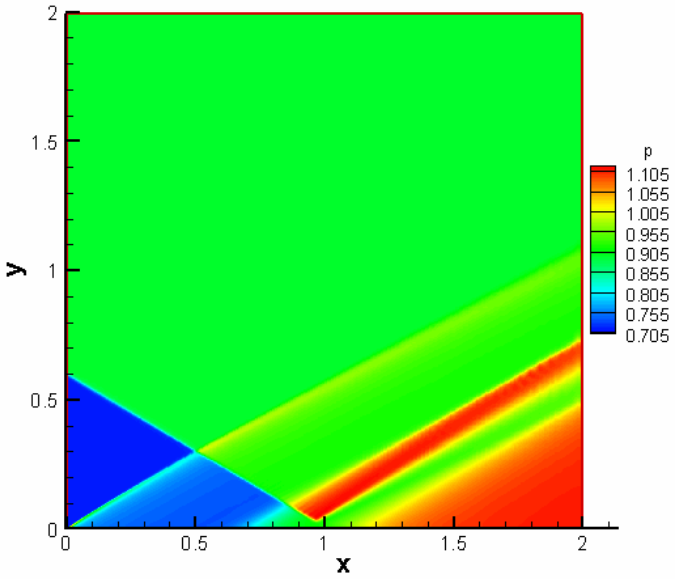

Figure 5.15 Pressure Contour: normal view

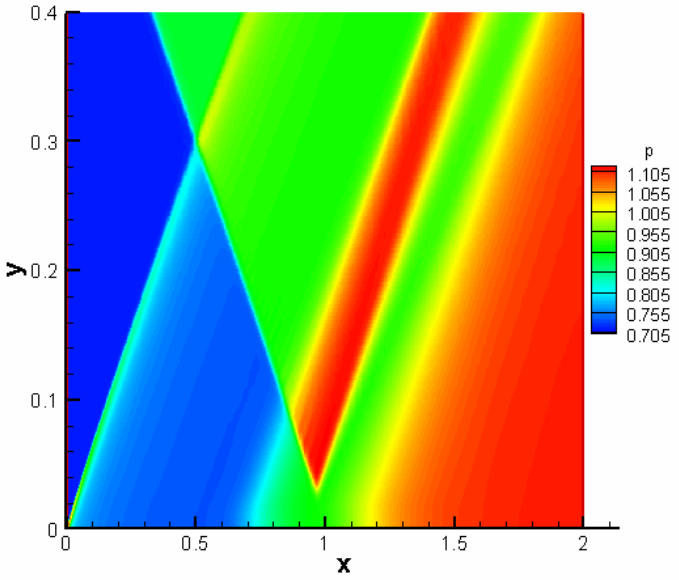

Figure 5.16 Pressure contour: vertically stretched by a factor of 5

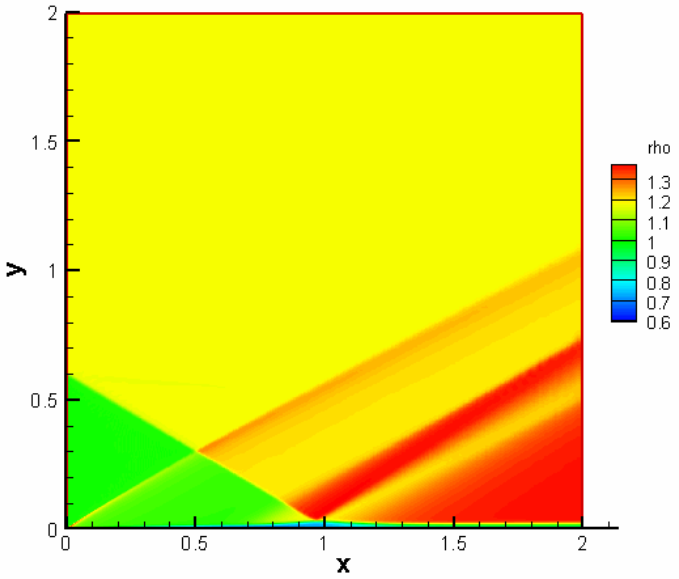

Figure 5.17 Density Contour : Normal View

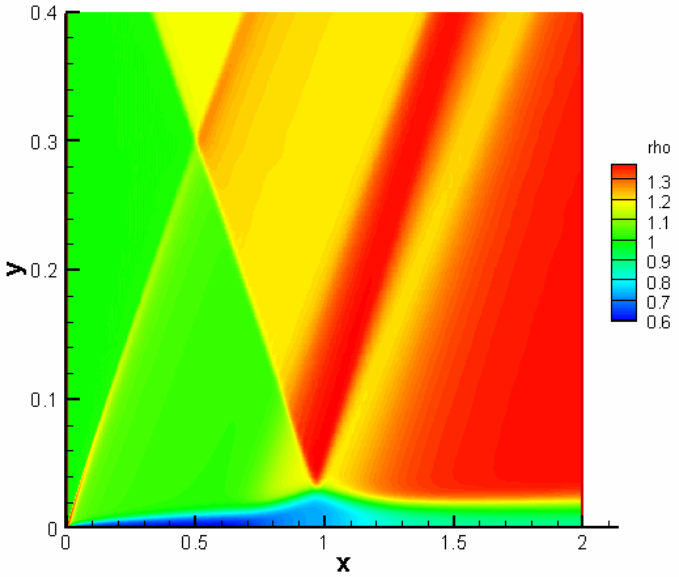

Figure 5.18 Density contour : vertically stretched by a factor of 5

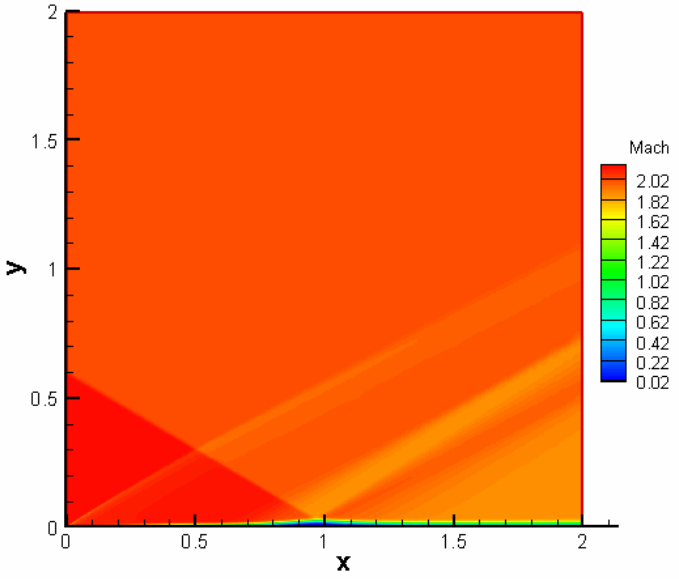

Figure 5.19 Mach Number Contour : Normal View

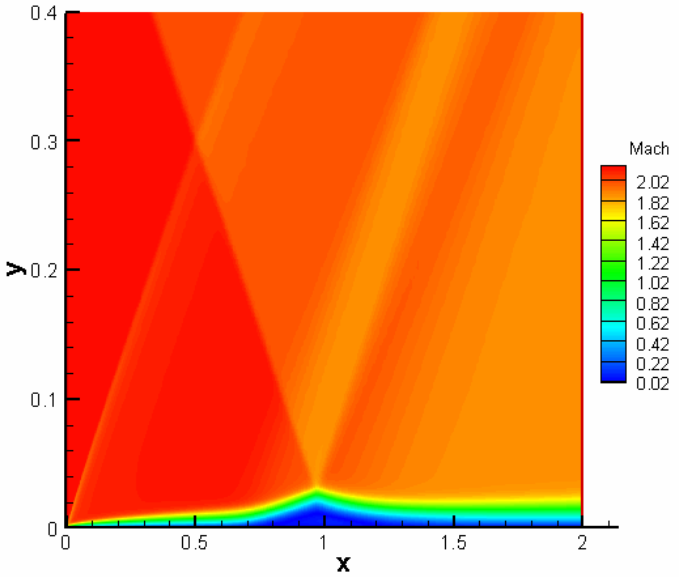

Figure 5.20 Mach Number Contour : Vertically Stretched by a factor of 5

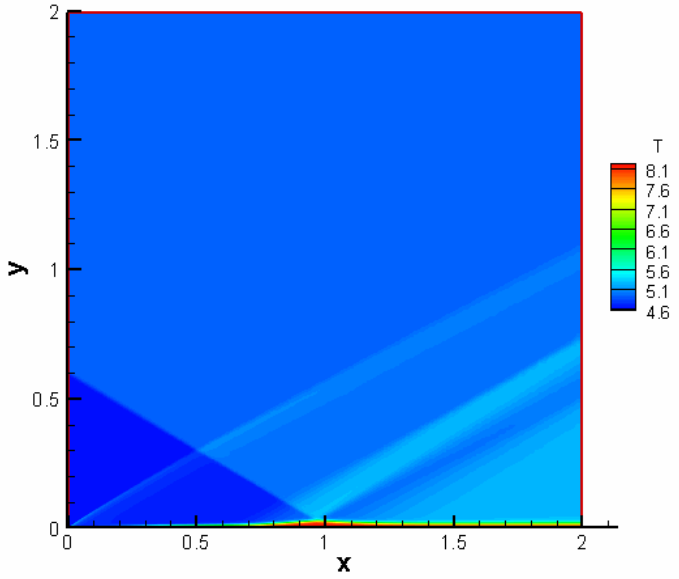

Figure 5.21 Temperature Contour : Normal View

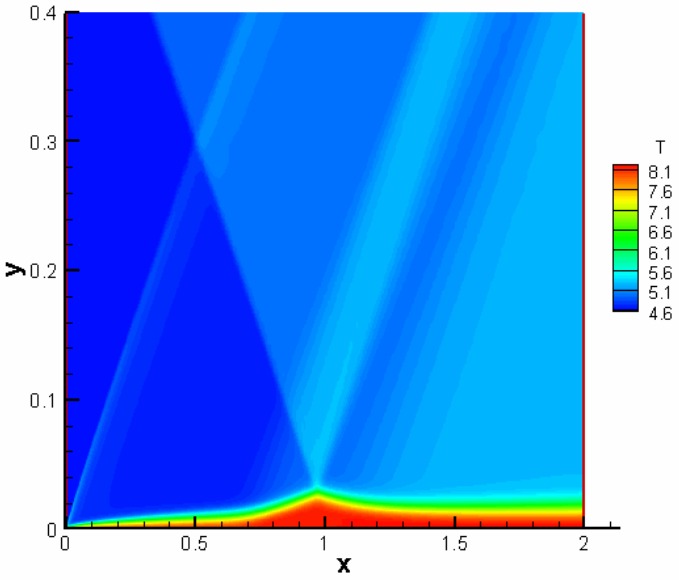

Figure 5.22 Temperature Contour : Vertically stretched by a factor of 5

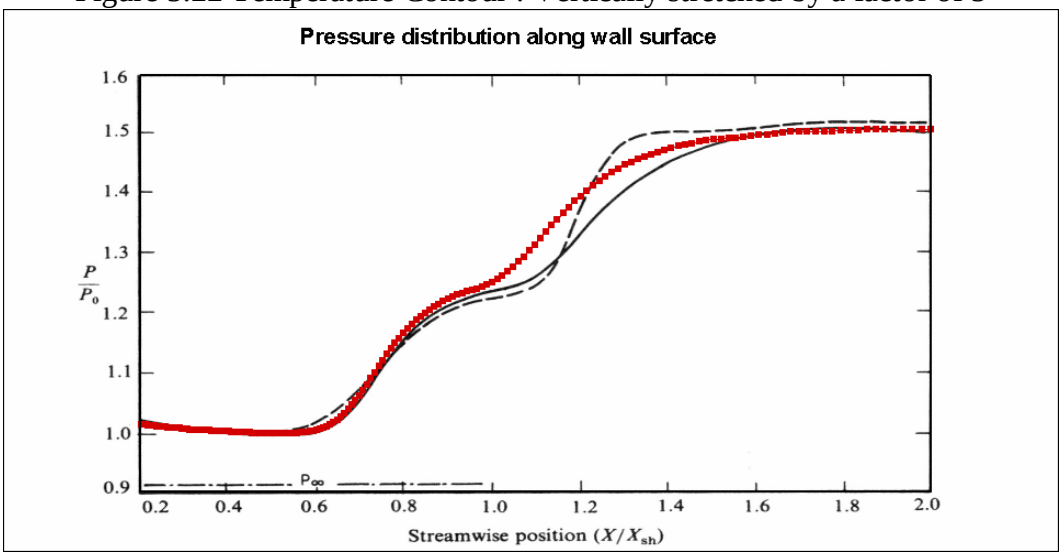

Figure 5.23 Comparison of pressure distribution on the wall surface.
(The red dots are our computation, the black dash one and solid one are Degrez's computation and experiment respectively.)

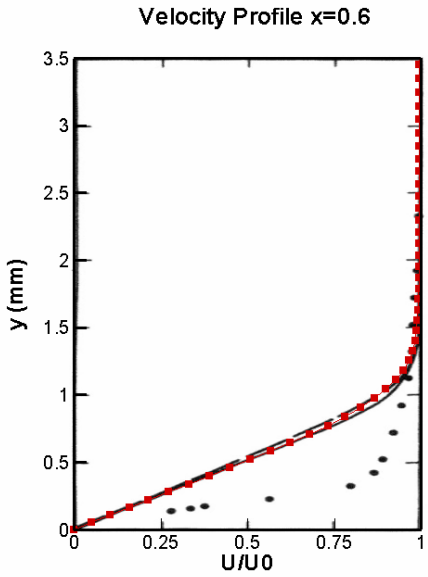

Figure 5.24 Comparison of velocity profiles at x=0.6
(The red dots are our computation, the black solid line and black dots are Degrez's computation and experiment respectively.)

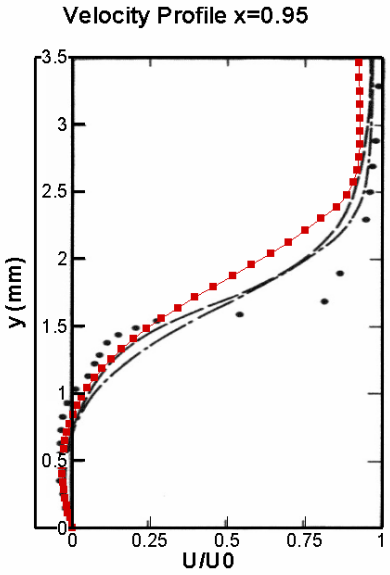

Figure 5.25 Comparison of velocity profiles at x=0.95
(The red dots are our computation, the black solid line and black dots are Degrez's computation and experiment respectively.)

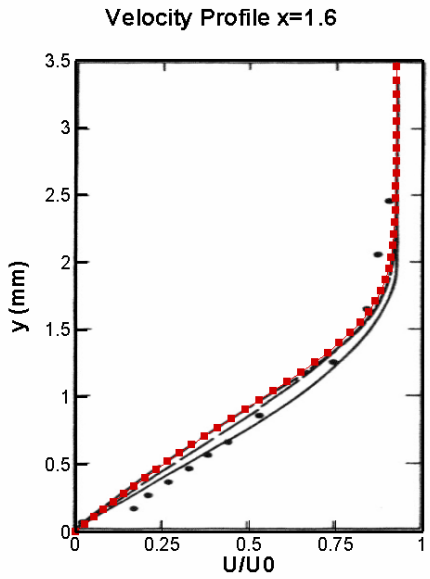

Figure 5.26 Comparison of velocity profiles at x=1.6
(The red dots are our computation, the black solid line and black dots
are Degrez's computation and experiment respectively)

Figures 5.15 – 5.22 show the distribution of pressure, density, Mach number and temperature obtained by our computation. Figures 5.23 – 5.26 show our numerical results agree well with the numerical results and are close to the experimental results given by Degrez et al (1987). Degrez et al favor their computational results addressed in their JFM paper.

5.4 Hypersonic flow around double angle

5.4.1 Flow parameters

In order to validate our scheme and code, we compared our results with well documented experimental and computational data. The case including the geometry and inflow condition was set same as the experiment conducted by Wadhams et al (2004) and the computation by Gaitonde et al (2002). The inflow Mach number is set to M=9.58, the Reynolds number Re=278870, the inflow temperature Tin=185.6, and the wall temperature Tw=293.3.

5.4.2 Numerical grid generation

Before we work on a double cone, a supersonic flow passing a double angle was solved first. The overall Grid is 257x129 obtained by elliptic grid generation and the girds are uniform in stream-wise direction, but stretched in wall normal direction with a factor of 1.037.

An elliptic grid generation method first proposed by Spekreijse (1995) is used to generate 2D grids. The elliptic grid generation method is based on a composite mapping, which is consisted of a nonlinear transfinite algebraic transformation and an elliptic transformation. The algebraic transformation maps the computational space C onto a parameter space P, and the elliptic transformation maps the parameter space on to the physical domain D. The computational space, parameter space, and the physical domain are illustrated in Figure 5.27. and the elliptic transformation maps the parameter

space on to the physical domain D. The computational space, parameter space, and the physical domain are illustrated in Figure 5.27. The computational space C is defined as the unit square in a two-dimensional space with Cartesian coordinates (x,h), and $x \in [0,1]$, $h \in [0,1]$ (see Figure 5.27). The grids are uniformly distributed on the boundaries and in the interior area of the computational space. The mesh sizes are $\frac{1}{N_x - 1}$ in the x direction and $\frac{1}{N_h - 1}$ in the h direction, where N_x and N_h are the grid numbers in the corresponding direction. The parameter space P is defined as a unit space in a two-dimensional space with Cartesian coordinate (s,t), and $s \in [0,1]$, $t \in [0,1]$. The boundary values of s and t are determined by the grid point distribution in the physical domain.

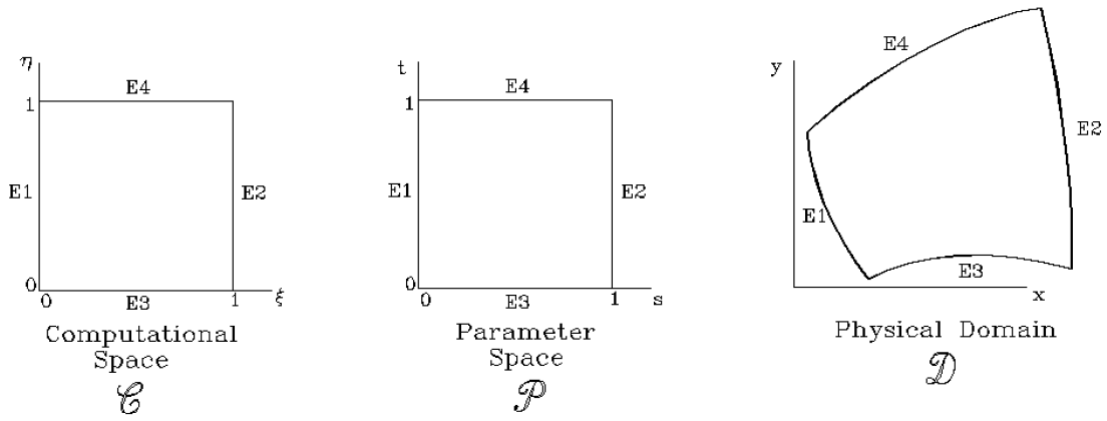

Figure 5.27 Computational Space C, Parameter Space P and Physical D

An algebraic transformation $s: C \rightarrow P$ is defined to map the computational space C onto the parameter space P. The grid distribution is specified by this algebraic

transformation, which depends on the prescribed boundary grid point distribution. The interior grid point distribution inside the domain, generated by the algebraic transformation, is a good reflection of the prescribed boundary grid point distribution.

Let $s_{E_3}(x) = s(x,0)$ and $s_{E4}(x) = s(x,1)$ denote the normalized arc-length along edges E_3 and E_4, $t_{E_1}(h) = t(0,h)$ and $t_{E_2}(h) = t(1,h)$ denote the normalized arc-length along edges E_1 and E_2. The algebraic transformation $s: C \rightarrow P$ is defined as

$$\begin{aligned} s &= s_{E_3}(\xi)(1-t) + s_{E_4}(\xi)t \\ t &= t_{E_1}(\eta)(1-s) + t_{E_2}(\eta)s \end{aligned}$$

which is called the algebraic straight line transformation. It defines a differentiable one-to-one mapping because of positiveness of the Jacobian $s_x t_h - s_h t_x > 0$.

The elliptic transformation $x: P \rightarrow D$, which is independent of the prescribed boundary grid point distribution, is defined to map the parameter space P onto the physical domain D. The elliptic transformation is equivalent to a set of Laplace equations

$$\begin{aligned} s_{xx} + s_{yy} &= 0 \\ t_{xx} + t_{yy} &= 0 \end{aligned}$$

The elliptic transformation defined by the above equations is also differentiable and one-to-one.

Till now we have defined two transformations, i.e., the algebraic transformation

s: $C \rightarrow P$, and the elliptic transformation *x*: $P \rightarrow D$. Because both the algebraic transformation and the elliptic transformation are differentiable and one-to-one, the composition the two transformation is also differentiable and one-to-one, so as to the inverse transformation.

In physical domain, the curvilinear coordinate system satisfies a system of Laplace equations:

$$\Delta \boldsymbol{r} = 0 \tag{5.1}$$

where $r = (x, y)^T$. The inherent smoothness of the Laplace operator makes the grids smoothly distributed in the physical domain. Being transformed to the computational space, this Laplace system becomes a set of Poisson equations. The control functions is determined by the composed transformation according to the following procedures. First, Equation 5.1 is transformed into the computational space *C*:

$$\begin{aligned} \Delta s &= g^{11} s_{\xi\xi} + 2g^{12} s_{\xi\eta} + g^{22} s_{\eta\eta} + \Delta\xi s_{\xi} + \Delta\eta s_{\eta} \\ \Delta t &= g^{11} t_{\xi\xi} + 2g^{12} t_{\xi\eta} + g^{22} t_{\eta\eta} + \Delta\xi t_{\xi} + \Delta\eta t_{\eta} \end{aligned}$$

where g^{11}, g^{12}, g^{22} are the components of the contravariant metric tensor, which can be calculated from the covariant metric tensor

$$\begin{aligned} g^{11} &= \frac{1}{J^2} g_{22} = (\boldsymbol{r}_{\eta}, \boldsymbol{r}_{\eta})/J^2 \\ g^{12} &= -\frac{1}{J^2} g_{12} = -(\boldsymbol{r}_{\xi}, \boldsymbol{r}_{\eta})/J^2 \\ g^{22} &= \frac{1}{J^2} g_{11} = (\boldsymbol{r}_{\xi}, \boldsymbol{r}_{\xi})/J^2 \end{aligned}$$

$\boldsymbol{J}$ is defined as $\sqrt{\det[g_{ij}]}$.

Then we have

$$\begin{pmatrix} \Delta\xi \\ \Delta\eta \end{pmatrix} = g^{11}\mathbf{P}_{11} + 2g^{12}\mathbf{P}_{12} + g^{22}\mathbf{P}_{22}$$

where

$$\begin{aligned} \mathbf{P}_{11} &= \begin{pmatrix} P_{11}^{(1)} \\ P_{11}^{(2)} \end{pmatrix} = -\mathbf{T}^{-1} \begin{pmatrix} s_{\xi\xi} \\ t_{\xi\xi} \end{pmatrix} \\ \mathbf{P}_{12} &= \begin{pmatrix} P_{12}^{(1)} \\ P_{12}^{(2)} \end{pmatrix} = -\mathbf{T}^{-1} \begin{pmatrix} s_{\xi\eta} \\ t_{\xi\eta} \end{pmatrix} \\ \mathbf{P}_{22} &= \begin{pmatrix} P_{22}^{(1)} \\ P_{22}^{(2)} \end{pmatrix} = -\mathbf{T}^{-1} \begin{pmatrix} s_{\eta\eta} \\ t_{\eta\eta} \end{pmatrix} \end{aligned}$$

and the matrix **T** is defined as

$$\mathbf{T} = \begin{pmatrix} s_\xi & s_\eta \\ t_\xi & t_\eta \end{pmatrix}$$

Then the Laplace system is transformed to the computational space *C*:

$$g^{11}\boldsymbol{r}_{\xi\xi} + 2g^{12}\boldsymbol{r}_{\xi\eta} + g^{22}\boldsymbol{r}_{\eta\eta} + \Delta\xi\boldsymbol{r}_\xi + \Delta\eta\boldsymbol{r}_\eta = 0$$

Δx and Δh are replaced by the control functions, then we obtain the Poission equations for the grid generation as follows,

$$g^{11}\boldsymbol{r}_{\xi\xi} + 2g^{12}\boldsymbol{r}_{\xi\eta} + g^{22}\boldsymbol{r}_{\eta\eta} + (g^{11}P_{11}^{(1)} + 2g^{12}P_{12}^{(1)} + g^{22}P_{22}^{(1)})\boldsymbol{r}_\xi + (g^{11}P_{11}^{(2)} + 2g^{12}P_{12}^{(2)} + g^{22}P_{22}^{(2)})\boldsymbol{r}_\eta = 0$$

where the control functions are defined by the algebraic transformation.

The elliptic transformation is carried by solving a set of Poisson equations. The control functions are specified by the algebraic transformation only and it is, therefore, not needed to compute the control functions at the boundary and to interpolate them into the interior of the domain, as required in the case for all well-known elliptic grid generation systems based on Poisson systems.

The computed grids are in general not orthogonal at the boundary. The algebraic transformation can be redefined to obtain a grid which is orthogonal at the boundary. First, redefine the elliptic transformation by imposing the following boundary conditions for s and t:

- $s = 0$ as edge E_1 and $s = 1$ at edge E_2.
- $\partial s/\partial \boldsymbol{n} = 0$ along edges E_3 and E_4, where $\boldsymbol{n}$ is the outward normal direction.
- $t = 0$ as edge E_3 and $t = 1$ at edge E_4.
- $\partial t/\partial \boldsymbol{n} = 0$ along edges E_1 and E_2, where $\boldsymbol{n}$ is the outward normal direction.

Second, redefine the algebraic transformation s : $C \rightarrow P$ according to two algebraic equations,

$$\begin{aligned} s &= s_{E_3}(\xi)H_0(t) + s_{E_4}(\xi)H_1(t) \\ t &= t_{E_1}(\eta)H_0(s) + t_{E_2}(\eta)H_1(s) \end{aligned}$$

where H_0 and H_1 are cubic Hermite interpolation functions defined as

$$H_0(s) = (1+2s)(1-s)^2$$
$$H_1(s) = (3-2s)s^2$$

Grid orthogonality at boundaries is obtained in three steps.

1. Compute an initial grid based on the Poisson grid generation system with control functions specified according to the algebraic straight line transformation defined by Eq.5.1;
2. Solve the two Laplace equations given by Eq.5.1 with the above specified boundary conditions;
3. Re-compute the grid based on the Poisson system but with control functions specified according to the algebraic transformation defined by Eq.5.1.

The grid details are shown below.

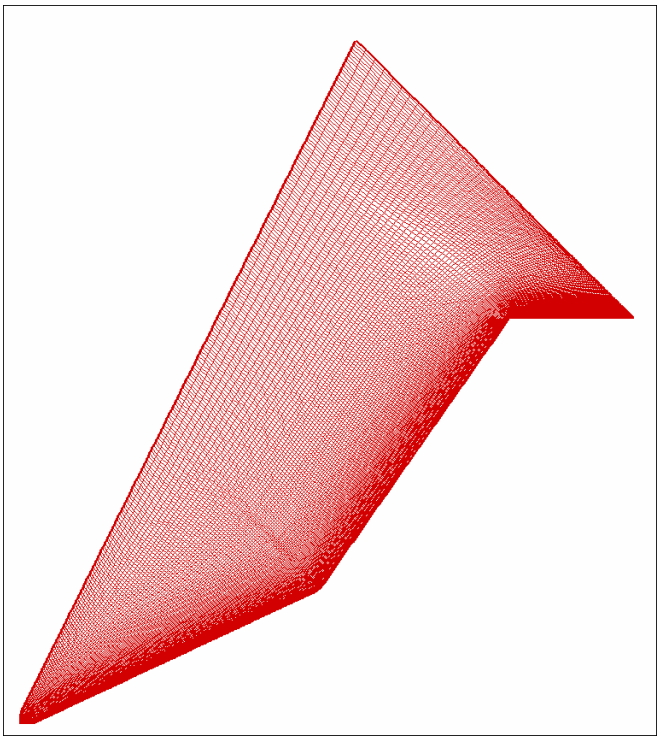

Figure 5.28 Overall Grid 257x129

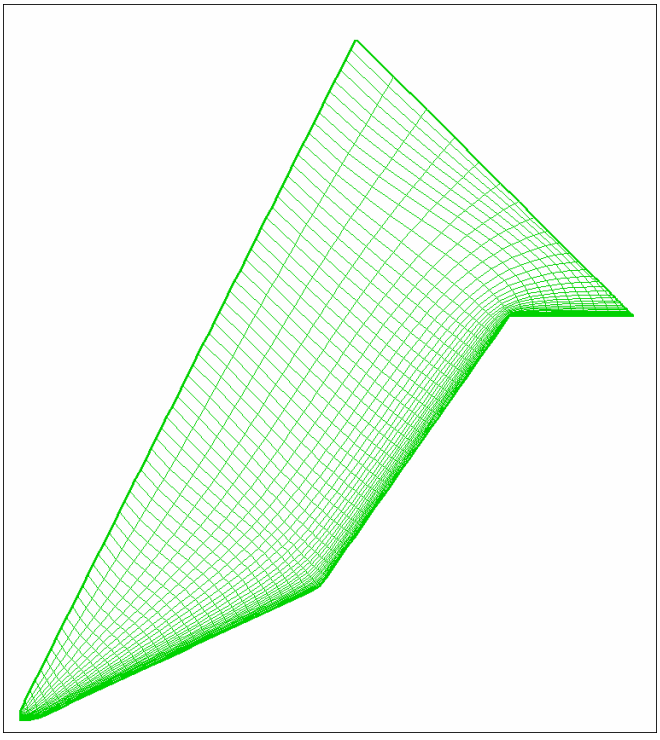

Figure 5.29 Coarse grid drawn every four points for illustration purpose (64x32)

Figure 5.30 Leading Edge

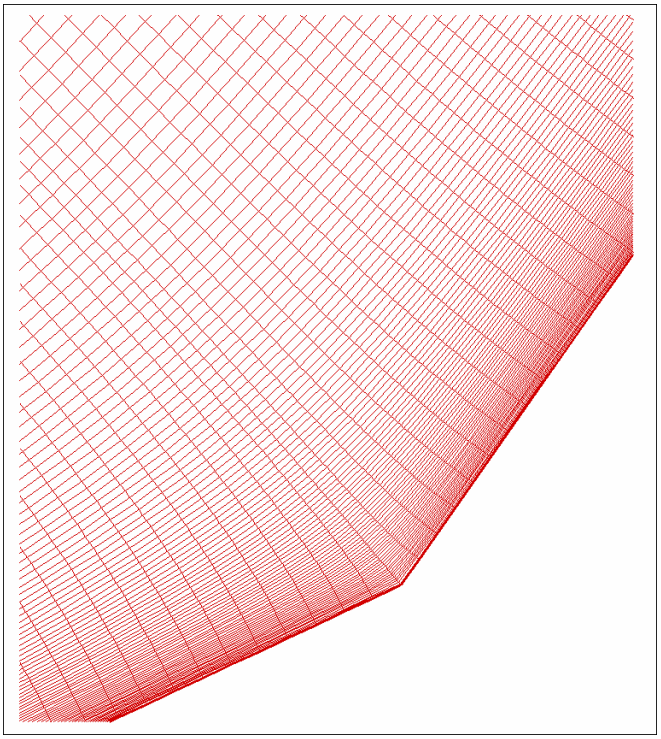

Figure 5.31 First Corner

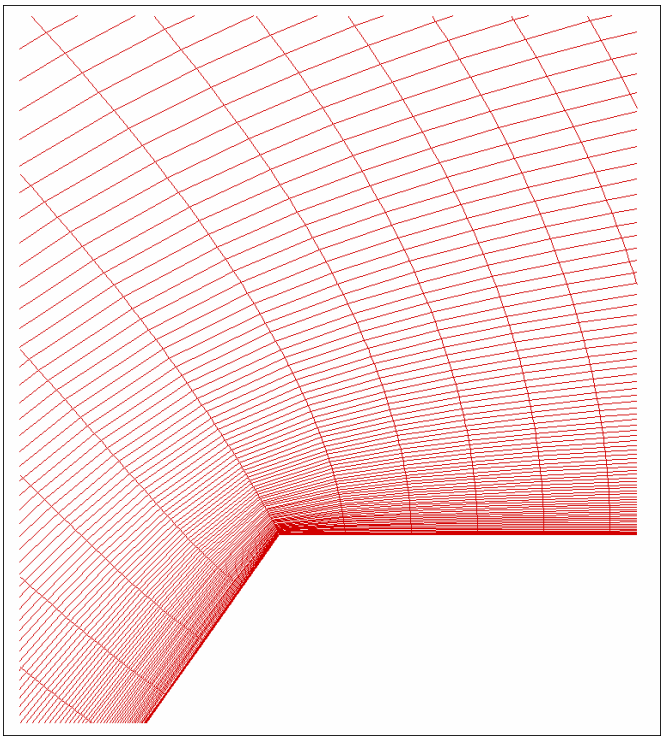

Figure 5.32 Second corner

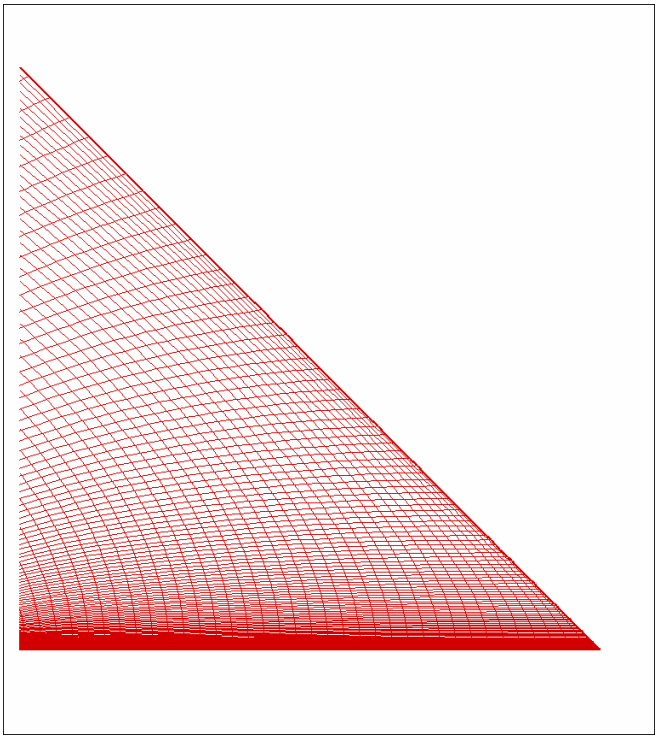

Figure 5.33 Trailing Edge

5.4.3 Preliminary results

The contour of flow field and distribution of physical quantities along the wall boundary are shown in Figure 5.39 — 5.41. Since the case we calculated is for a double angle not a double cone, we cannot compare with the above experiment and computation directly for now. However, the distribution of Mach number, pressure, density, and temperature are very similar.

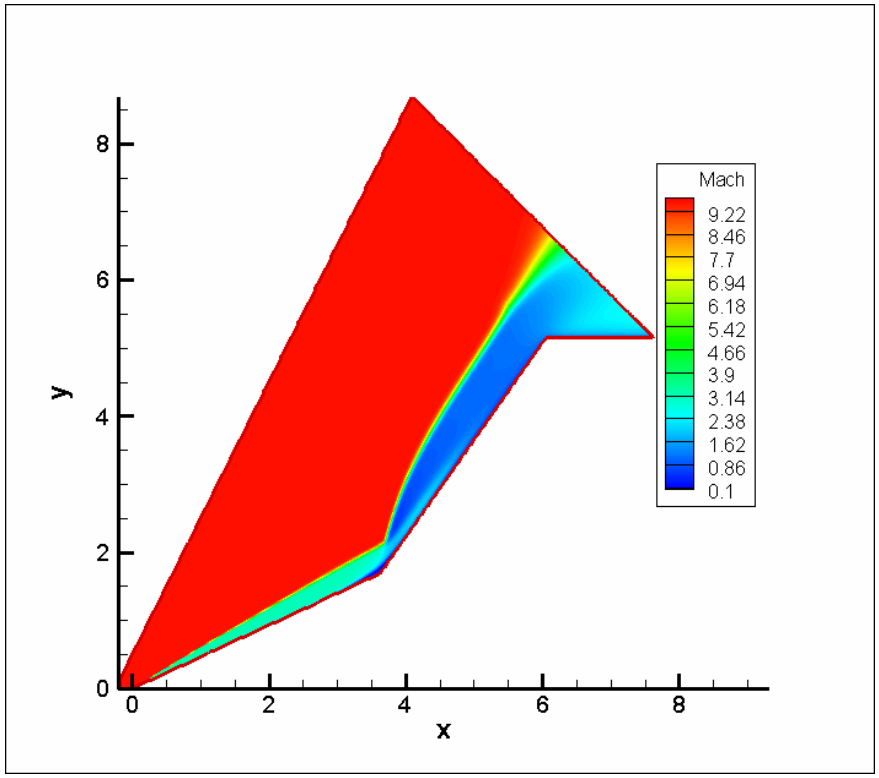

Figure 5.34 Contours of Mach Number

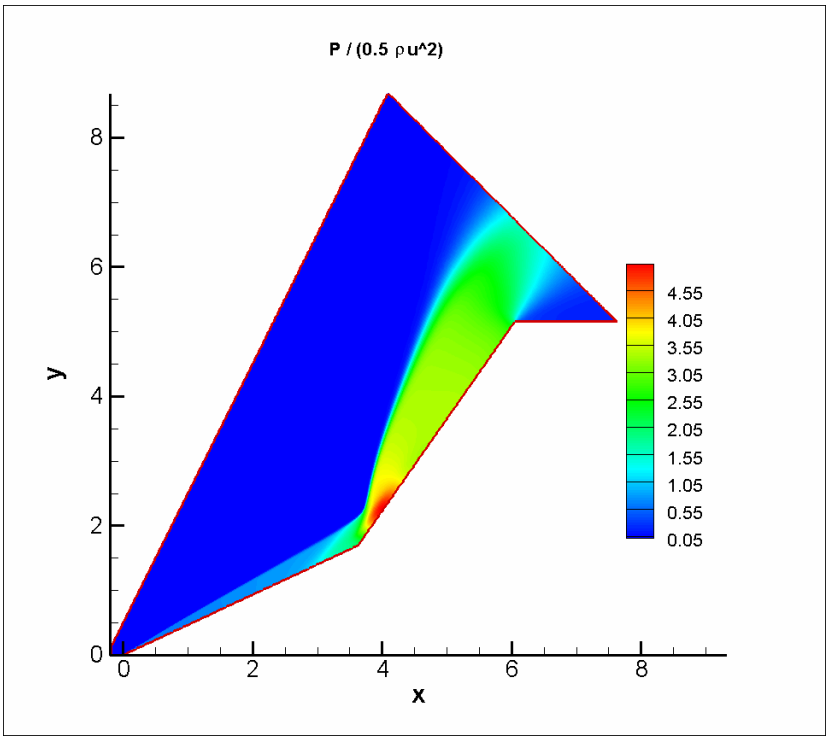

Figure 5.35 Contours of Pressure

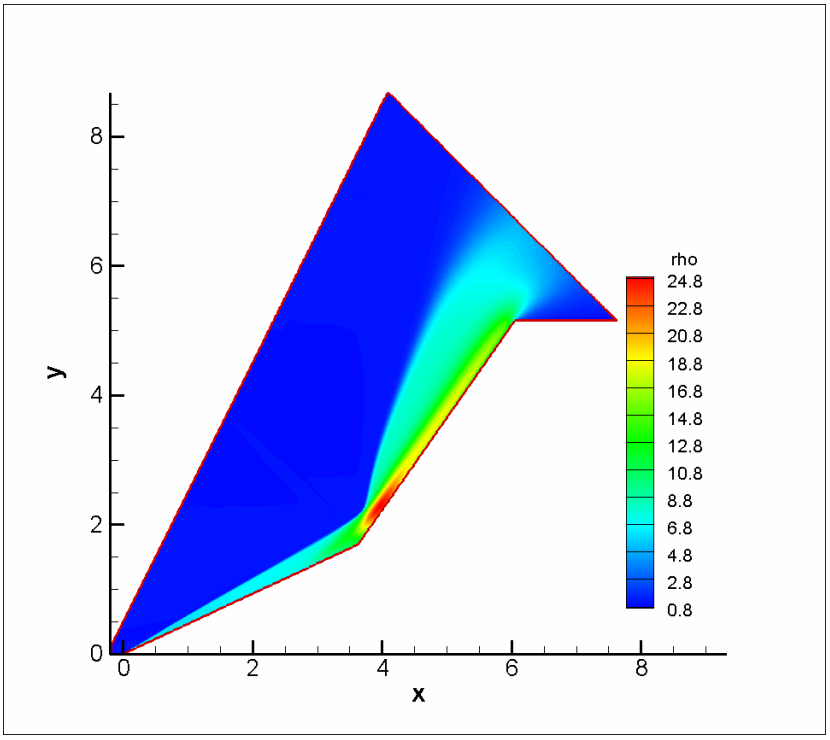

Figure 5.36 Contours of Density

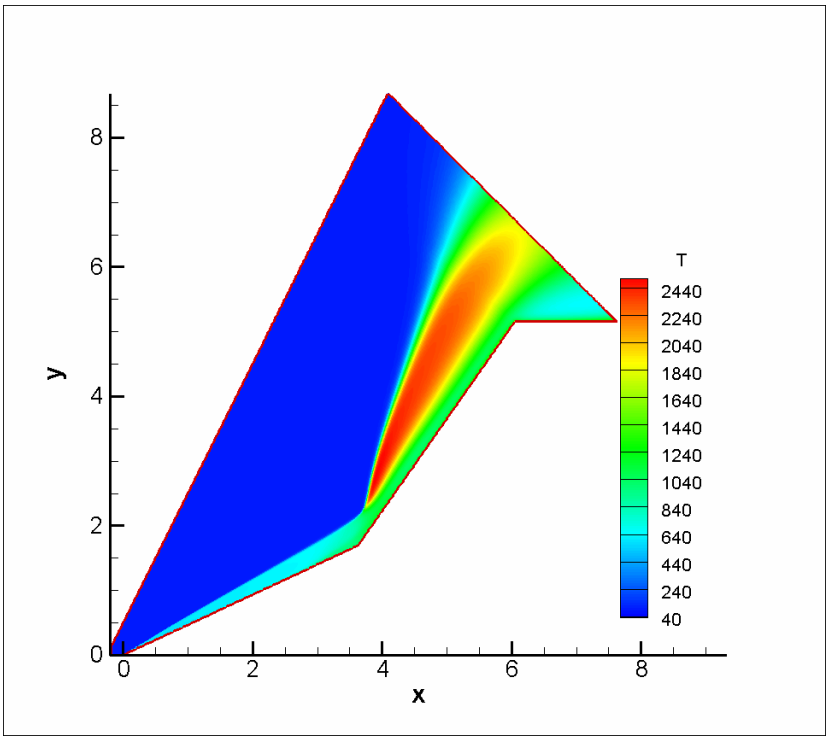

Figure 5.37 Contours of Temperature

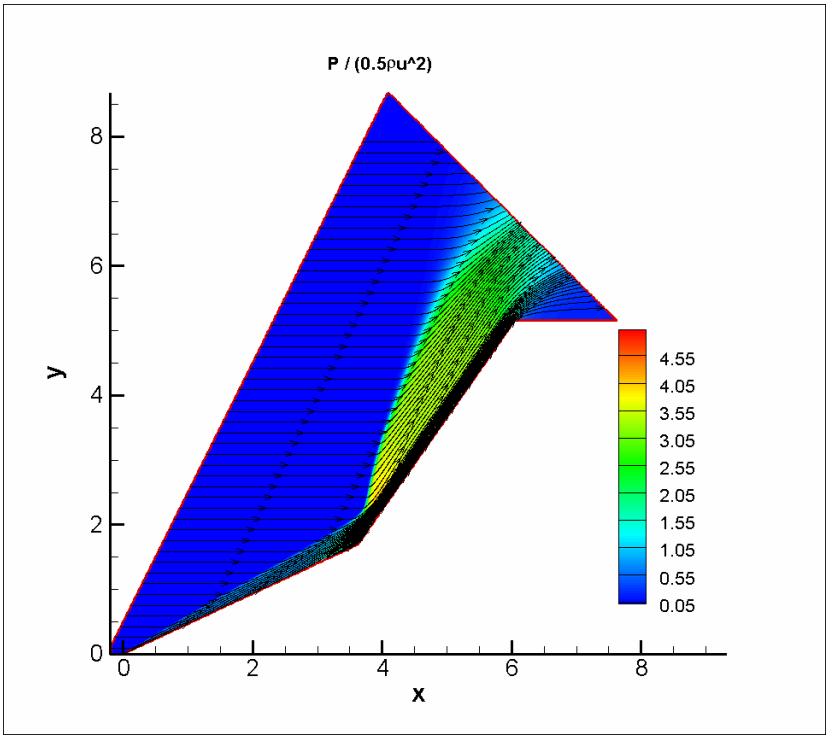

Figure 5.38 Pressure Contours with Streamlines

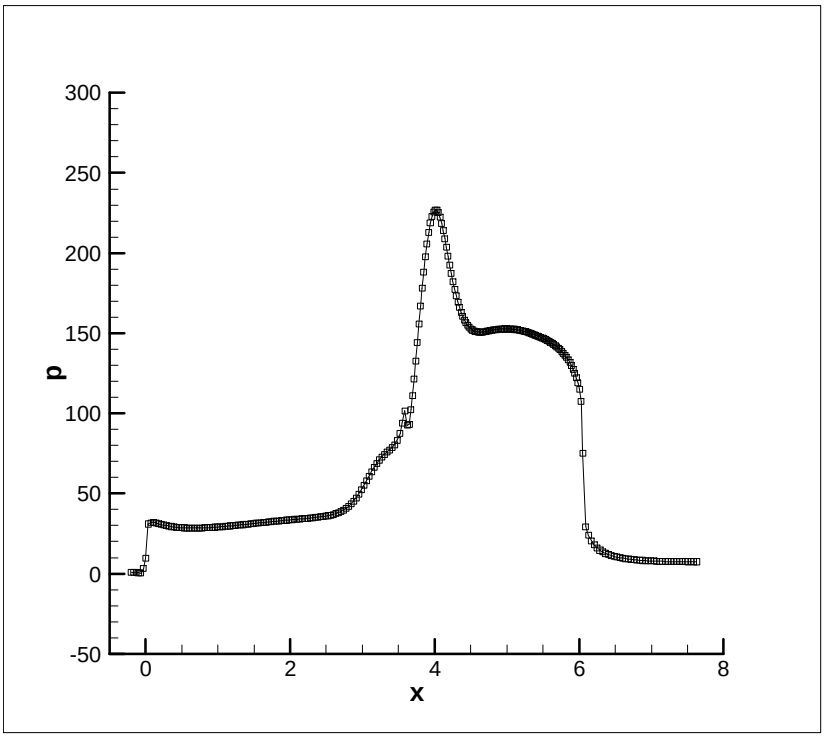

Figure 5.39 Pressure Distribution Along Wall Surface

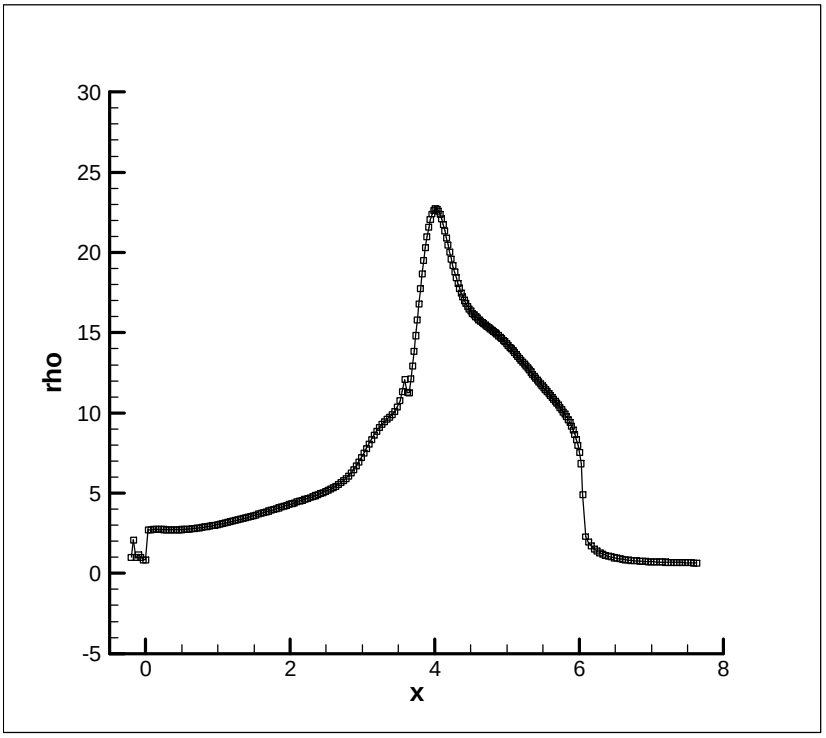

Figure 5.40 Density Profile Along Wall Surface

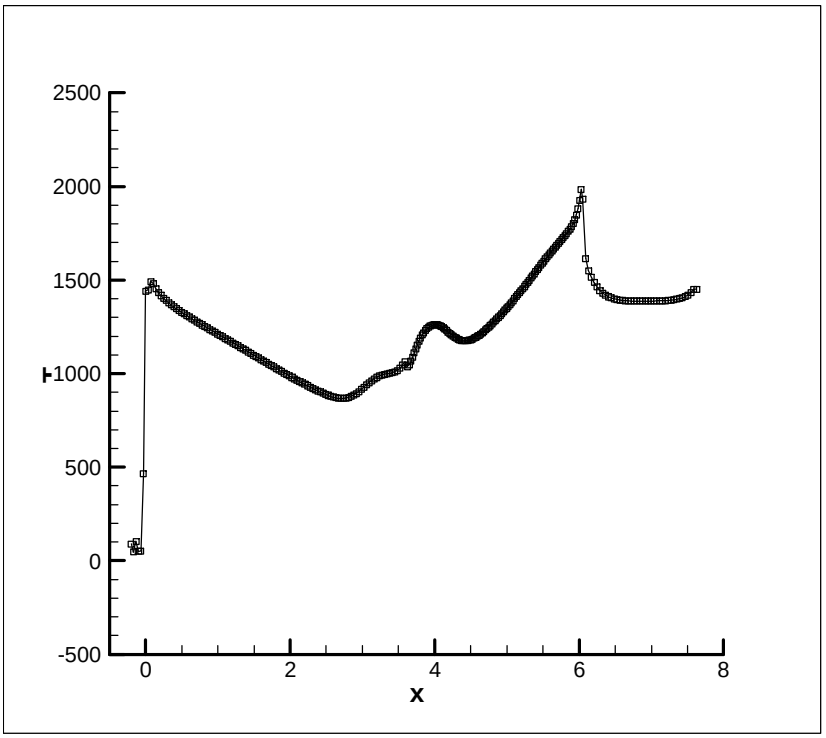

Figure 5.41 Temperature Profile Along Wall Surface

Although we used same geometry and inflow conditions as the experiment (Wadhams et al, 2004) and the computation used, we cannot directly compare our results with theirs since their results are for double cones and ours for double angles. However, we can make qualitatively comparison and find the flow structure is very similar. Figure 5.42 – 5.45 show such a comparison

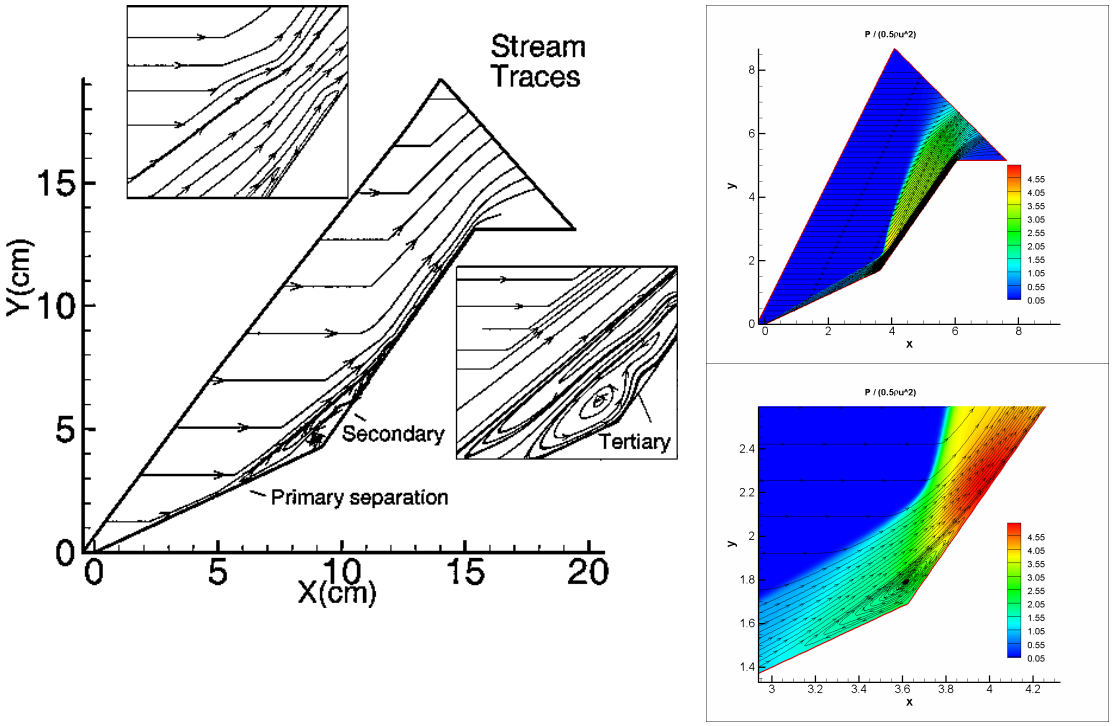

Computation by Gaitonde et al, 2002 Liu et al, 2007

Figure 5.42 Qualitative comparison of streamline and separation bubble

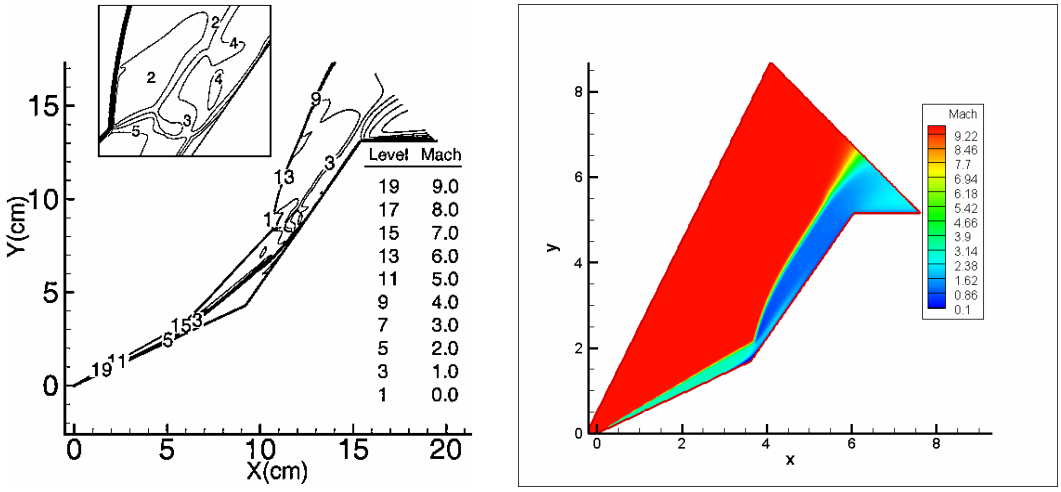

Computation by Gaitonde et al, 2002 Liu et al, 2007

Figure 5.43 Qualitative comparison of Mach number

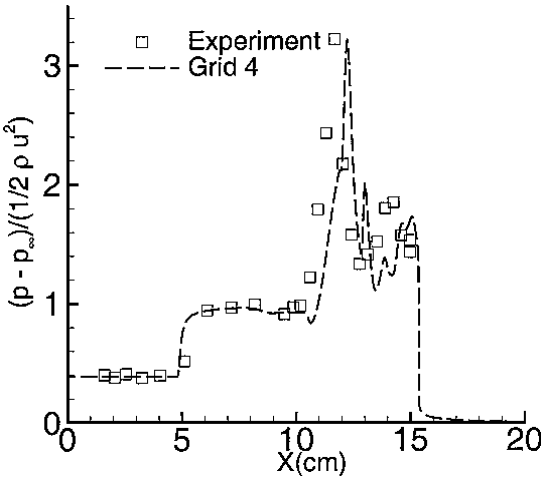

Experiment (Wadhams et al, 2004) and Computation (Gaitonde et al, 2002)

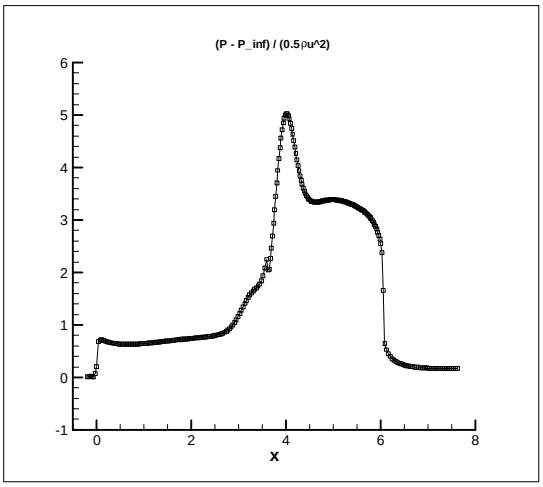

Liu et al, 2007

Figure 5.44 Qualitative comparison of *Cp*

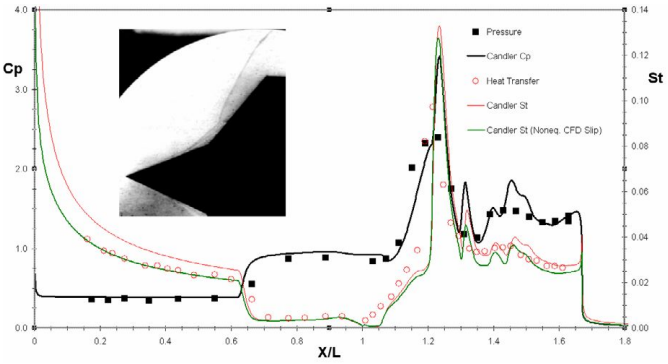

Experiment (Wadhams et al, 2004)

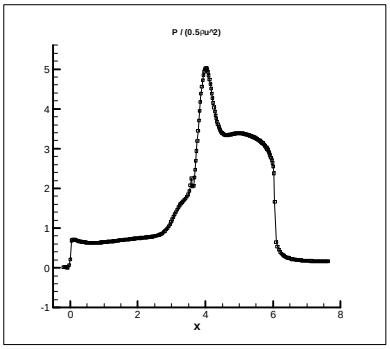

Liu et al, 2007

Figure 5.45 Qualitative comparison of pressure distribution

CHAPTER 6

CONCLUSIONS AND DISCUSSIONS

In this work, a uniform weighted compact / non-compact scheme with 6th order of accuracy (UWCNC-6) is developed based on our previous Weighted Compact Scheme (WCS). The behaviors and properties of UWCNC are studied. It is further applied to one- and two-dimensional Euler equations as well as two-dimensional Navier-Stokes equations. Based on the numerical results, the following conclusions are made,

1. The UWCNC-6 scheme uses a uniform formulation for both compact and non-compact schemes. The global dependency of the scheme is determined by the parameter a which is calculated based on smoothness.
2. The new UWCNC scheme has the capability of capturing shocks in both one and two dimensions. In most cases, shocks and contact surfaces are captured sharper than WENO-5 results.
3. The central differencing and high order of accuracy make UWCNC-6 less dissipative than WENO-5. This property is desirable when small scale structures are very important.

4. The simulation of shock / boundary layer interaction shows that UWCNC-6 has better resolution inside boundary layer where the N-S equation is largely parabolic:
    a. In many cases the separation region has many small-scale structures (vortices). UWCNC-6 resolves these small vortices better than WENO-5 does.
    b. In other cases where the flow is proven to be steady and laminar, UWCNC-6 also resolves the flow field; the numerical solution matches the previous work in literatures.
5. The simulation of hypersonic flow around double angle shows that UWCNC-6 has the capability of capturing very strong shocks (M>9). This makes it very promising in the future study of hypersonic boundary layer, transition, shock / boundary layer interaction, etc where both shock and small vortices are present in the flow field simultaneously.

REFERENCES

[1] Gaitonde, D, and Visbal, M, Pade-type high-order boundary filters for the Navier-Stokes equations, AIAA Journal, Vol. 38, No. 11, pp 2103-2112, 2000.

[2] Gaitonde, D, Canupp, p. W., and Holden, M., Heat transfer predictions in a laminar hypersonic viscous/inviscid interaction, Journal of thermophysics and heat transfer, Vol. 16, No. 4, October–December 2002

[3] Godunov, S. K., A difference scheme for numerical computation of discontinuous solution of hydrodynamic equations, Math Sbornik, Vol 47, 271-306 (in Russian) translated US Joint Publ. Res. Service, JPRS 7226, 1969.

[4] Harten A, High resolution schemes for hyperbolic conservation laws, J. of Computational Physics, Vol 49, pp357-393, 1983.

[5] Harten A, Engquist B, Osher, B, Charkravarthy SR, Uniformly high order accurate essentially non-oscillatory schemes III, J. of Computational Physics, Vol 71, pp231-303, 1987.

[6] Jiang, G. S., Shu, C. W., Efficient implementation of weighted ENO scheme. J. Comput. Phys., 126, pp.202—228, 1996.

[7] Jiang L, Shan H, Liu C, Weight Compact Scheme for Shock Capturing, International Journal of Computational Fluid Dynamics, 15, pp.147-155, 2001.

[8] Lele S.K., Compact finite difference schemes with spectral-like resolution, Journal Computational Physics, 103, pp.16—42, 1992.

[9] Liu, C., Xie, P., and Olveira, M, High order modified compact scheme for high speed flow, technical report to Gaitonde at Air Force Research Lab.

[10] Liu, D, Osher, S, Chan, T, Weighted essentially nonoscilltory schemes, J. of Computational Physics, V115, pp200-212, 1994

[11] Roe, P.L., Approximate Riemann solvers, parameter vectors and difference schemes, J. of Computational Physics, Vol 43, pp357-372, 1981

[12] Shu, C.W., Osher, S., Efficient implementation of essentially non-oscillatory shock-capturing scheme. Journal of Computational Physics 77, pp.439-471, 1988.

[13] Shu, C. W., Osher, S., Efficient implementation of essentially non-oscillatory shock-capturing schemes II, J. Comput. Phys.,83, pp.32-78, 1989.

[14] Spekreijse, S.P., Elliptic Grid Generation Based on Laplace Equations and Algebraic Transformations. Journal of Computational Physics 118, pp.38-61, 1995.

[15] Su, Xie, Oliveira, and Liu, Error Analysis for Weighted Higher Order Compact Finite Difference Scheme, J. of Applied Mathematical Science, to appear.

[16] Van Leer, B., Towards the ultimate conservative difference scheme. V. A second order sequel to Godnov's scheme, Journal of Computational Physics, Vol 32, pp101-136, 1979

[17] Visbal, M. and Gaitonde, D., On the use of higher-order finite-difference schemes on curvilinear and deforming mashes' JCP, Vol. 181, pp155-158, 2002.

[18] Wadhams, T. P., Holden, M. S., Summary of experimental studies for code validation in the LENS facility with recent Navier-Stokes and DSMC solutions for two- and three- dimensional separated regions in hypervelocity flows, AIAA 2004-917 42nd AIAA Aerospace Sciences Meeting and Exhibit, 5 - 8 January 2004, Reno, Nevada

BIOGRAPHICAL INFORMATION

Peng Xie was born in the city of Liaoyang, Liaoning province, P.R. China in 1979. He moved to the city of Hefei, Anhui in 1997 and entered the University of Science and Technology of China for undergraduate study. He majored in fluid mechanics. Under the supervision of Professor Zhaoyuan Han, he graduated in 2001 with a bachelor's degree in Theoretical and Applied Mechanics. He wrote his bachelor's thesis, titled "Experimental Techniques in The Combination Operation of Shock Tube and Shock Tunnel".

He continued his graduate study in the University of Science and Technology of China. In 2004, under the supervision of Professor Zhaoyuan Han, he obtained a master's degree in fluid mechanics. His thesis was titled "A study of the interaction between two triple-points".

In August 2004, he entered the University of Texas at Arlington to pursue doctoral study in applied mathematics. Under the supervision of Dr. Chaoqun Liu, his study focused on the numerical simulation of shock / boundary layer interaction. His dissertation was titled "Uniform Weighted Compact / Non-compact Schemes for Shock / Boundary Layer Interaction".